Microstructure Evolution Mechanism of Single and Multi-pass in Laser Cladding Based on Heat Accumulation Effect for Invar Alloy

Shichao Zhu (zhushichao888@126.com)
Nanjing University of Aeronautics and Astronautics
Chenxiao Yu
Anhui University of Technology
Zhen chang
Hangzhou Bearing Test & Research Center Co.,Ltd
Xiaohong Zhan
Nanjing University of Aeronautics and Astronautics
Chao Zeng
Guizhou Institute of Technology

Research Article

Keywords: Laser cladding, Invar alloy, Microstructure evolution mechanism, Heat accumulation effect

Posted Date: April 27th, 2021

DOI: https://doi.org/10.21203/rs.3.rs-340039/v1

Microstructure Evolution Mechanism of Single and Multi-pass in Laser Cladding Based on Heat Accumulation Effect for Invar Alloy

Shichao Zhu[1*], Chenxiao Yu[2], Zhen Chang[3], Xiaohong Zhan[4*], Chao Zeng[5]

1. College of Aeronautics and Mechanical Engineering, Changzhou Institute of Technology, Changzhou, 213002, P.R. China

2. College of Metallurgical Engineering , Anhui University of Technology, Maanshan, 243032, P.R. China

3. Hangzhou Bearing Test & Research Center Co.,Ltd, Hangzhou, 310022, P.R. China

4. College of Material Science and Technology, Nanjing University of Aeronautics and Astronautics, Nanjing 211106, P.R. China

5. College of Aerospace Engineering, Guizhou Institute of Technology, Guiyang 550003, P.R. China

Abstract: This work explores how the process parameters in laser cladding affect the evolution of the microstructure of the single pass and multi-pass cladding layers of Invar alloys. The research examined the cladding layers from three aspects: (1) the transformation of grain size, HAZ width, ratio of the columnar crystal to the equiaxed crystal, and change of Fe content of cladding layer; (2) the effects of heat accumulation on grain size, HAZ width and remelting zone; and (3) the hardness distribution of single pass and multi-pass cladding layers. The investigation has the following four findings: (1) the cladding layer is composed of equiaxed crystals at the top and columnar crystals at the bottom of cladding layer; (2) the processing parameters have significant effects on the width of the HAZ, proportion between the columnar and equiaxed crystals and the change of Fe content of cladding layer. (3) the gradual accumulation of heat causes the increase in HAZ width, the grain size, and the area of the remelting zone; and (4) the hardness progressively reduces from the top to bottom along the direction of the centerline of the cladding layer.

Keywords Laser cladding; Invar alloy; Microstructure evolution mechanism; Heat accumulation effect

1 Introduction

The laser cladding is an advanced additive fabricating technology. The laser beam shines on and melts the particles and the surface of the substrate, and fuse them together. The laser beam, as a heat source, melts the powder particles as they are ejected out of the nozzle, and creates a molten pool on the substrate. The fusion and diffusion leave an excellent bonding in between [1, 2]. The laser cladding exhibits many advantages: less heat input, smaller heat-affected zone (HAZ), lower thermal deformation and dilution rate, fast cooling rate, perfect metallurgy bonding between the cladding layer and substrate, wonderful mechanical properties, high-precision geometrical characteristics of cladding layer, and facilitation in automation contrasting with the traditional welding procedure [3, 4]. Hence, the marvelous idea is to provide various powder particles over the damaged surfaces to return to desired size and shape. So, the laser cladding can be employed for a good many of parts, varying from oil and gas, aerospace, automobile, defense, mould and nuclear industries [5, 6].

The extensive use of the Invar alloy mould may create a myriad of problems in the aviation

* Corresponding author: E-mail: zhushichao888@126.com, xiaohongzhan_nuaa@126.com

manufacturing: such as shrinking, undercutting, porosity, cracking in the welding assembly, and exceeding dimension tolerance, abrasion, material fatigue in the manufacturing and using. Thus, an appropriate remanufacturing technology that can fix the damaged or worn parts would be needed to recycle the mould, thereby cutting the production costs and protecting the environment [7, 8]. In contrast to the conventional method, which repairs the damaged parts with laser welding, not without defects in the welding layer, the proposed laser cladding has a lot to recommend itself [9-12].

In recent years, a great deal of investigation on laser cladding has been discussed for the evolution mechanism of the microstructure. To improve the bearing surface nature of the water-lubricated guiding bearing, Deng et al. [13] explored the effect of power on microstructure, abrasion, cross-sectional hardness gradient, and corrosion resistance of cladding layer by laser cladding. The results show that the different laser powers had effects on the structure size of cladding layer and element distribution. Xu et al. [14] researched the evolutions of microstructure and mechanical behaviors of HAZ. They characterized the microstructure of HAZ through the OM and SEM and measured the hardness distribution of cladding layer by Vickers hardness tester. The maximum temperature of thermal cycle plays a significant effect on the evolution of microstructure and behaviors of HAZ. With the reduction of the maximum temperature, the solid-state transformation temperature, elongation and impact energy increase, while the hardness decrease. Zhan et al. [15] investigated the influences of heat input on the size, microstructure and porosity of cladding layers for Invar alloy through optical and scanning electron microscopy, electronic differential system (EDS). The results presented that the microstructure of cladding layers comprise elongate cellular crystals and equiaxed cellular crystals. Their research discussed that the size, HAZ and crystals size of cladding layer and substrate show a noteworthy increase by increasing heat input. Dinda et al. [16] analysed the structure and properties of cladding layer by optical microscope (OM), scanning electron microscope (SEM), X-ray diffraction and hardness test. They found the microstructure of the cladding layer is columnar dendritic in nature, which grew epitaxially from the substrate. Zhan et al. analyzed the effect of different process parameters on morphology of cladding layer and also quantified the microstructure and width of the HAZ for Invar alloy. Tarak et al. [17] considered that the influence of technology parameters of subsequent cladding layers on the microstructure and mechanical behavior of cladding layers to select desired process parameters and characterize the influence. The results show that the microstructure of the top layer was equiaxed, while the near substrate zone was fine dendritic. Moreover, the speed and power have a considerable influence on microstructure and hardness of cladding layers. In summary, the laser cladding for Invar alloy mould is infrequent, so the relations among technology parameters and microstructure evolution are far from being completely established. Therefore, it is necessary appropriate process parameters to realize the desired evolution of microstructure and hardness of cladding layer and substrate.

However, a quantitative research into the microstructure and thermal process of the cladding layers is essential to the investigation of the microstructure in laser cladding process, because it will provide significant reference for precise repair of Invar alloy mould. In this paper, the evolution mechanism of the microstructure of laser cladding for Invar alloy is analysed quantitatively. The content are as follow: (1) the transformation of grain size, HAZ width, ratio of the columnar crystal to the equiaxed crystal, and change of Fe content of cladding layer; (2) the effects of heat accumulation on grain size, HAZ width and remelting zone; and (3) the hardness distribution of single pass and multi-pass cladding layers. In addition, the correlations between process parameters

and microstructure characteristics of cladding layer are further established.

2 Experiment

2.1 Experimental Material

The Invar alloy substrate in this experiment was produced by the French Pulang Alloy Co., Ltd. and was supplied by Commercial Aircraft Corporation of China Ltd. Next, upon the experimental requirements, the substrate was processed with the dimension of: 100 mm × 50 mm × 20 mm. Besides, the powder particles were fabricated through the plasma rotating electrode. The chemical compositions of substrate and particles are illustrated in Table 1. The thermophysical properties of the Invar alloy were presented in Table 2. The elemental composition of the particles was detected via energy-dispersive X-ray spectroscopy, as presented in Fig. 1(a). The morphological (size and shape) of the powder was detected with SEM, and the radius of the particles were performed to be in the size range of 60–140 μm, as presented in Fig. 1(b).

Table 1 Elemental composition of Invar alloy

Chemical composition	S	C	Mn	Fe	Ni	Cr	Co	Si	P
wt%	0.001	0.025	0.27	63.0	35.92	0.20	0.47	0.07	0.0087

Table 2 Thermophysical properties of Invar alloy

Elongation	Hardness	Density	Tensile strength	Thermal conductivity	Modulus of elasticity
δ/%	HV	g−cm^{-3}	σ_b/MPa	W · (m−K)$^{-1}$	MPa
30	140	8.12	500	0.109~0.134	134, 000

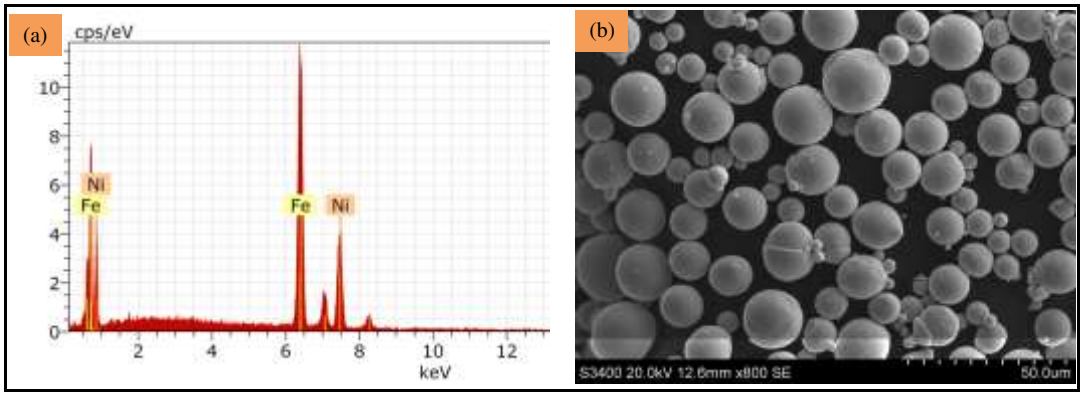

Fig. 1. Elemental composition and morphology of Invar alloy particles. (a) Elemental composition. (b) Morphology

2.2 Experimental equipment and methods

The laser cladding equipment employs a 6kW laser system (TRUMPF, Germany), a gas protection system, a powder particle feeding system, and a control system, as shown in Fig. 2. The cross-sections of the cladding layers were sliced with the wire-electrode cutting and then was ground, polished though the carborundum papers with different particle sizes after the laser cladding experiments. The expected testing and measuring of the non-contact optical instrument collects the geometric features on the width, height, and cross-sectional contour of cladding layer through the white light interferometry.

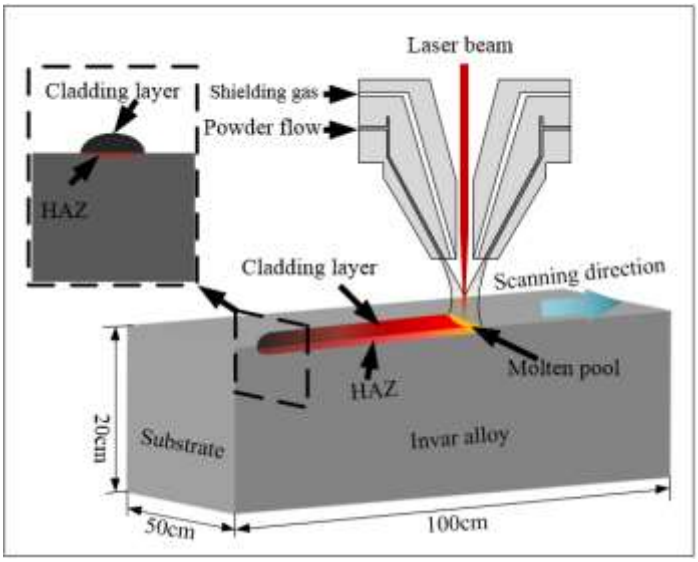

Fig. 2. Diagrammatic of laser cladding process

3. Results and analysis

3.1 Microstructural analysis of Invar alloy

Fig.3 presents the cross-sectional microstructure of the single-pass cladding layer for Invar alloy with the power of 2000 W, speed of 3 mm/s and feeding rate of 1.5 g/s. The sample was primarily composed of three regions, including the substrate, heat affected zone (HAZ), and cladding layer, as presented in Fig. 3(a). The boundary marked by the yellow dashed line between the HAZ and cladding layer is fusion line. The microstructure of substrate was composed of single-phase austenite, whose grain size was small (Fig. 3(b)). The microstructure in the HAZ was relatively coarse (Fig. 3(c)) due to the heat transfer. The grain in this area heated and the secondary growth occurred. The heat transferred from the surface to the substrate continuously decreased. Thus, the austenite grain size in this area gradually increased from the substrate to the fusion line. The cladding layer was above the fusion line, and consisted of the columnar crystals at the bottom and equiaxed crystals at the top. At the bottom of molten pool, the columnar crystal epitaxially grew inside the molten pool with grains in HAZ as the nucleation sites. To gain advantages in the competitive grain growth, the preferred growth direction of epitaxial columnar crystals was along the maximum temperature gradient, i.e. the normal direction of the fusion line. The subgrain structure was composed of the elongate crystals (Fig. 3(d)) and regular cellular crystals (Fig. 3(e)). The top of cladding layer mostly consisted of equiaxed crystals, while the subgrain structure was regular cellular crystals with different sizes (Fig. 3(f)).

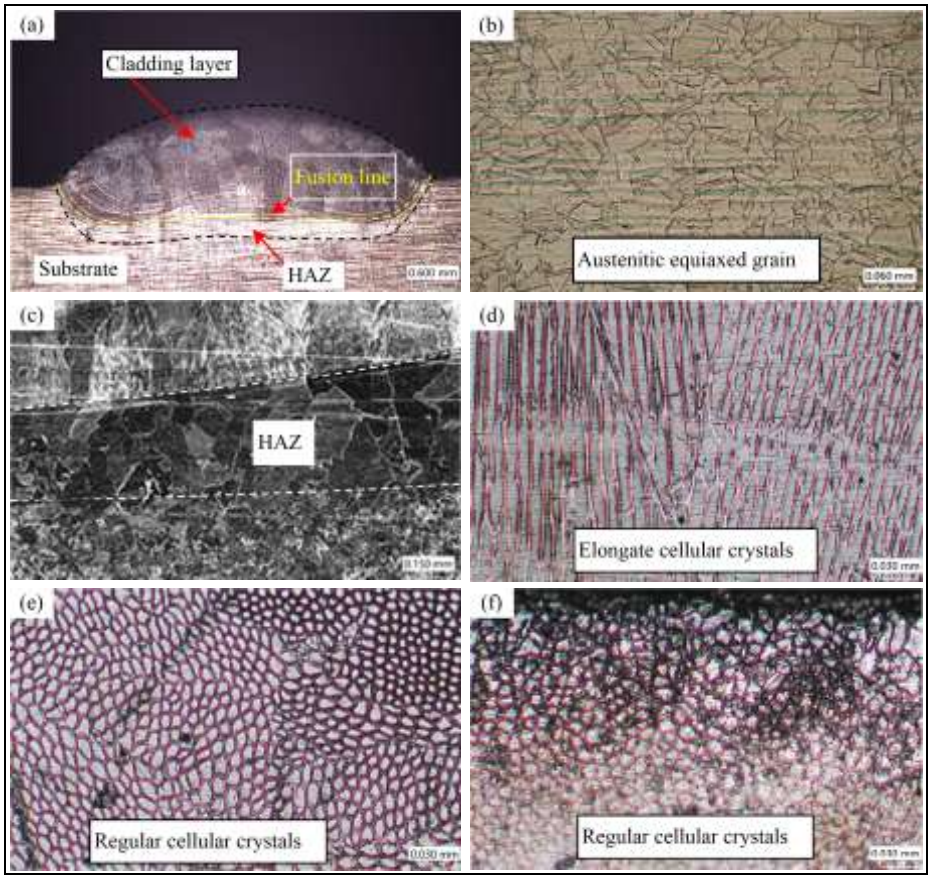

Fig. 3. Microstructures of different regions of single-pass cladding layer cross section: (a) cross-sectional microstructure; (b) substrate microstructure; (c) microstructure of heat affected zone; (d) microstructure at the bottom region of cladding layer; (e) microstructure at the bottom zone of cladding layer; (f) microstructure at the top region.

To further understand the subgrain morphology in the cladding layer, the microstructure of the longitudinal section along the scanning direction was investigated. The microstructure of the longitudinal section and 3-dimensional morphology and cross-sectional microstructure of subgrains are shown in Fig. 4. Most of the columnar crystals clearly grew along the white arrow from the fusion line to cladding layer surface and along the scanning direction at 20° angle with the vertical direction. The phenomenon primarily occurred because the laser movement made the maximum temperature on the longitudinal section of the molten pool shift along the scanning direction. Fig. 4(c) shows the 3-dimensional morphology of subgrains in area *c*, which displays long strip shape on the longitudinal section and round shape on the cross section. Therefore, the grain morphology in area *c* was elongated cellular subgrain. Also, as shown in Fig. 4(d), fine equiaxed cellular crystals were observed on the surface of the cladding layer. The 3-dimensional morphology of the subgrains in area *e* is presented in Fig. 4(e). Compared with the grains in area *c*, the grain morphologies on the cross section and longitudinal section of area *e* were both equiaxed crystals. Thus, the subgrains at the top of cladding layer were equiaxed subgrains.

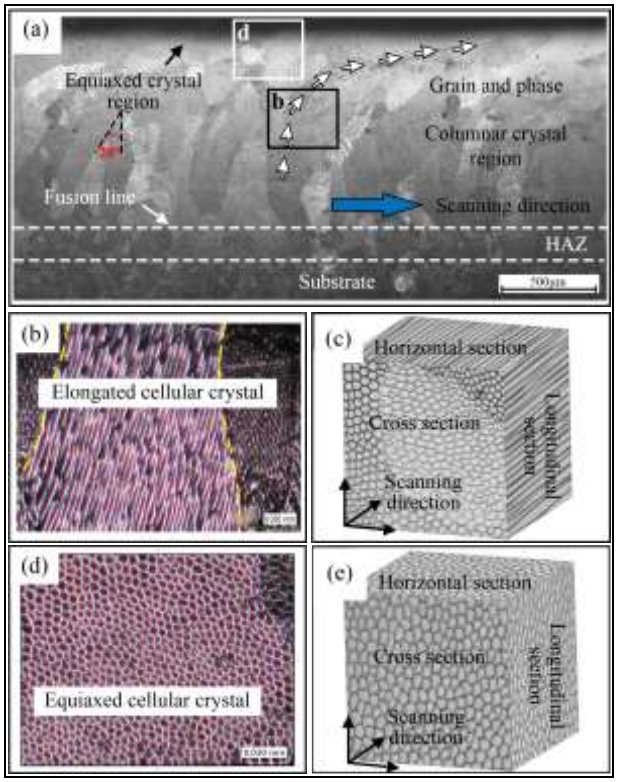

Fig. 4. Microstructure of longitudinal section of cladding layer: (a) microstructure of longitudinal section; (b) microstructure of central region; (c) 3-dimensional image of subgrains in central region; (d) microstructure at top region; (e) 3-dimensional image of subgrains at the top region.

The morphology and size of the columnar crystal at the bottom and the subgrain at the top were researched. The SEM images are presented in Fig. 5. There was not much precipitation phase at the top and bottom of cladding layer, and the grain boundary was clear. The measurements show that the average size of subgrains at the top was 772 μm, and the value of the subgrain at the bottom was 1204 μm, which is much larger than that at the top. These results can mainly be attributed to the sufficient grain growth conditions at the primary solidification stage of molten pool and continuous growth perpendicular to the fusion line. Meanwhile, due to enough space, the growth along the width direction was sufficient. However, at the later stage of solidification, the grain growth space was limited with the shrinkage of molten pool and the grain growth was slow, even the columnar to equiaxed transition (CET) occurred.

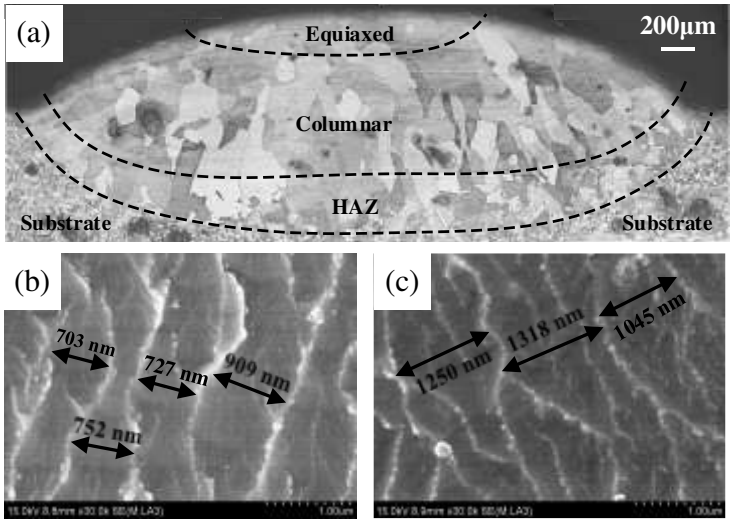

Fig. 5. SEM images of top and bottom of cladding layer cross section: (a) microstructure images; (b) SEM micrograph of top grains; (c) SEM micrograph of bottom grains.

The CET of local molten pool during the laser cladding process is shown in Fig. 6. The formations of columnar and equiaxed crystals were not simultaneous, but had a certain time sequence. Solidification first occurred at the bottom of molten pool. As the temperature decreased, the solidification moved from bottom to the center of molten pool. Therefore, at the initial solidification stage, the grains at the bottom of molten pool nucleated and grew with the grain at the HAZ as the nucleation sites. The grains displayed clear cogenetic crystallization characteristics, and they performed columnar morphology (Fig. 6(a)). As the temperature decreased, the columnar crystals continuously grew towards the center of molten pool. When the columnar crystals moved to a certain location of molten pool, the heat accumulated in the cladding layer and the temperature gradient and cooling rate decreased. Meanwhile, the supercooling degree at the center of the molten pool increased. When the overall cooling rate and temperature gradient near the molten pool further decreased to a relatively low value, the condition of equiaxed crystal nucleation was reached, and the homogeneous nucleation started. In addition, there might have been some un-melted cladding powders at the center of the final molten pool, which provided the conditions for the heterogeneous nucleation of equiaxed crystals, and the columnar to equiaxed transition (CET) occurred (Fig. 6(b)). With a decrease in temperature, the equiaxed crystals continuously grew. At the same time, the columnar crystals also continuously grew and moved forward until they met and solidification was complete (Fig. 6(c) and 6(d)).

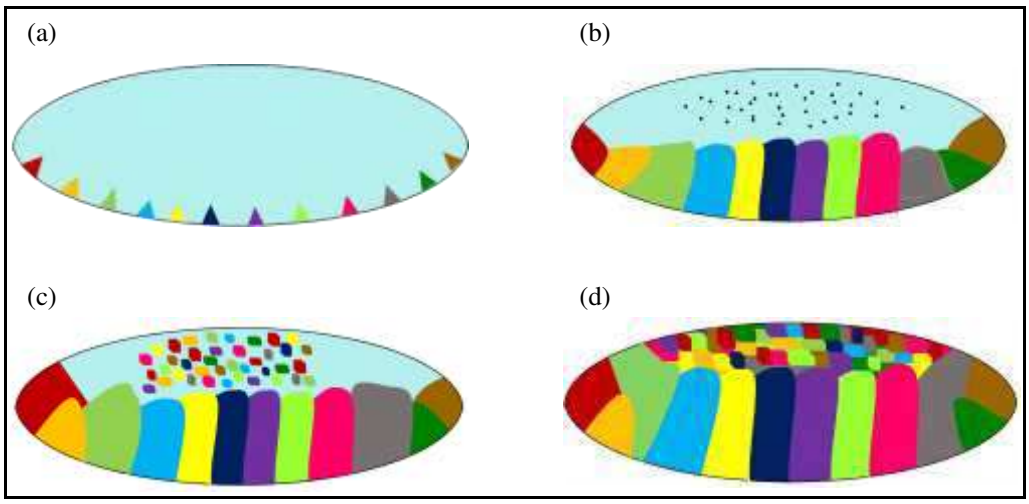

Fig. 6. Columnar-to-equiaxed transition (CET) process.

To further explored the microstructure evolution of the cladding layer, the EDS element detection schematic and results of the cross-sectional cladding layer are presented in Fig. 7. The elemental distribution in the cladding layer depends on the solute transfer at the liquid stage of the molten pool during the cladding process, which is closely correlated with the flow field. Therefore, the quantitative measurement of the elemental contents in the cladding layer can indirectly reflect the flow field features of molten pool. The sample with power of 2000 W, speed of 3 mm/s, and feeding rate of 1.5 g/s was selected. The EDS detection points were at the left half region of the cladding layer, and three points were near the cladding layer surface and three were inside the cladding layer. The detection points were annular and Fe was taken as the detected element. The detection results show that the maximum Fe content of 64.39 wt.% was present at Point 3 near the surface center of the cladding layer, and the minimum Fe content of 62.52 wt.% was present at Point 5 near the center region. Moreover, as per the change diagram of Fe content distribution, average Fe content near the surface was higher than that inside the cladding layer. This is because at the liquid stage of the molten pool, the Marangoni flow caused by surface tension and temperature gradient was mainly distributed at the upper half of the molten pool. The existence of the Marangoni flow significantly improved the solute transfer in the molten pool. Thus, the element distribution in this area was closely related to the Marangoni flow. Because of the viscosity of liquid metal, the flow velocity was different in different regions. On the one hand, because of the edge absorption effect on liquid metal, the flow velocity near the edge of the molten pool was slower. On the other hand, due to different temperatures in different areas of the molten pool, liquid metal flow velocities in different areas were different, which is manifested as low viscosity and high flow velocity in the high-temperature area, and vice versa, in the low-temperature area. In the molten pool, the flow velocity near the edge was lower than that in the inner area. The solute tended to accumulate at the edge area, leading to enrichment.

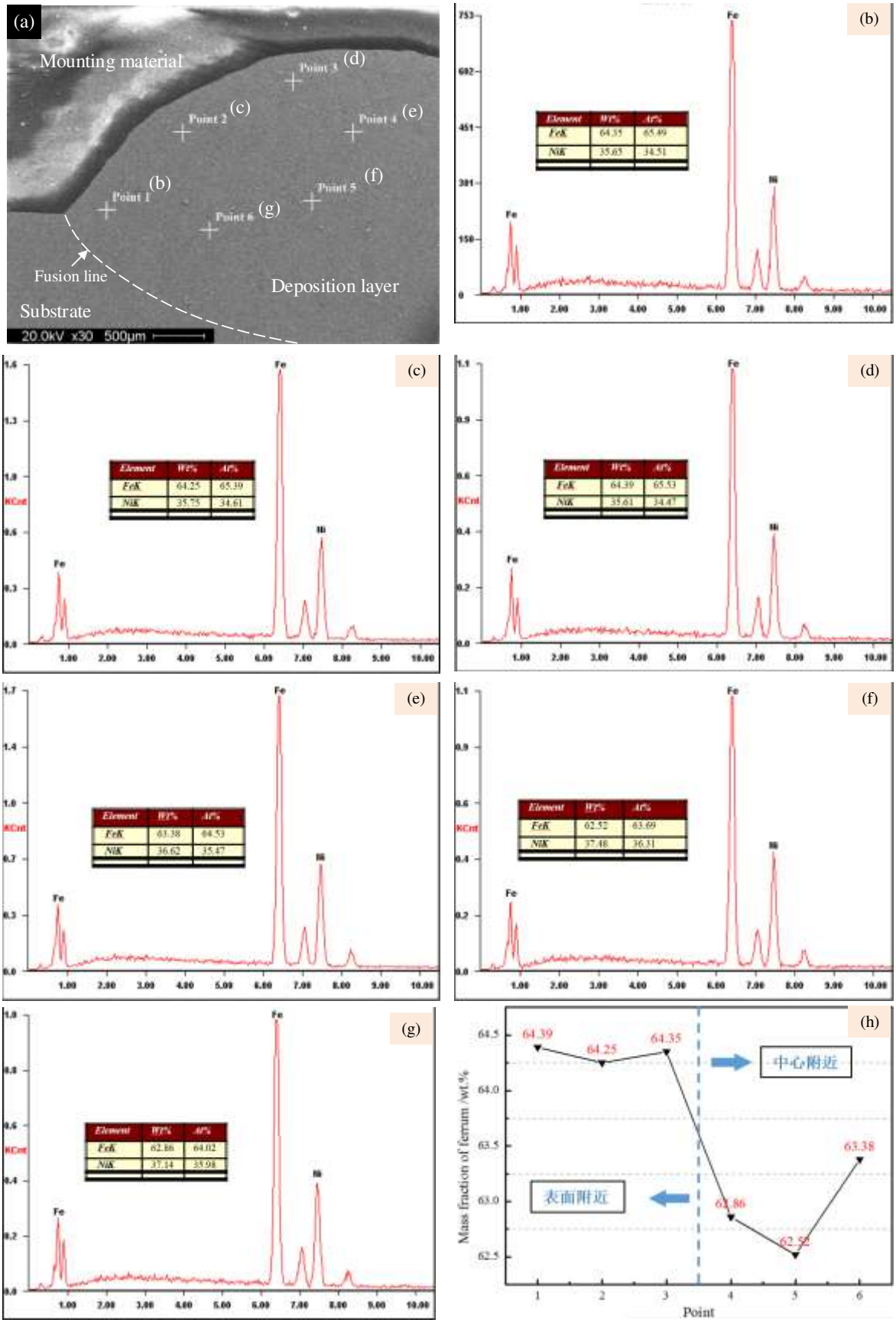

Fig. 7. EDS elemental measuring results of cladding layer cross section: (a) schematic diagram; (b) – (g) results of different measuring points; (h) variation curve of Fe content

3.2 Effects of process parameters on microstructure

The effects of processing parameters on the Invar alloy primarily included the width of HAZ, grain size, proportion of columnar and equiaxed crystals in the cladding layer, and Fe content change in the left half region of the cladding layer. At the constant powder feeding rate of 1.5 g/s, the single-pass laser cladding experiment was conducted by controlling the power and speed. Table 3 shows the processing parameters of the single-pass cladding. Herein, the linear energy density (LED) was employed to explore the influence of different processing parameters on the single-pass sample. The LED was computed with the following equation:

$$\eta = \frac{P}{v} \tag{1}$$

where P is the laser power and v is the scanning speed.

Table 3 Processing parameters of single-pass

No.	Laser power (W)	Scanning speed (mm/s)	Powder feeding rate (g/s)	Linear energy density (J/m)
1	2000	5	1.5	400
2	2300	5	1.5	460
3	2000	3	1.5	667
4	2300	3	1.5	767

The influence of different processing parameters on width of HAZ is shown in Fig. 8. The width of HAZ increased with an increase in LED. With the increase in LED from 400 J/m to 767 J/m, the width of HAZ significantly increased from 347 μm to 618 μm. The austenite grains in the HAZ were affected by the heat transfer of the molten pool, which led to the high-temperature thermal conditions for the grain growth in HAZ. Driven by the grain boundary interface curvature, the high-angle grain boundary moved and absorbed the surrounding grains, which reduced the number of grains and increased the average grain size. With a higher laser power, due to the large heat input, the temperature of molten pool was relatively high, which facilitated the grain growth in HAZ, and hence, an increase in HAZ width. When the scanning speed decreased, the interacting time between the power and substrate increased and the temperature increased, which endowed grains in HAZ enough time to grow, leading to an increase in width of HAZ.

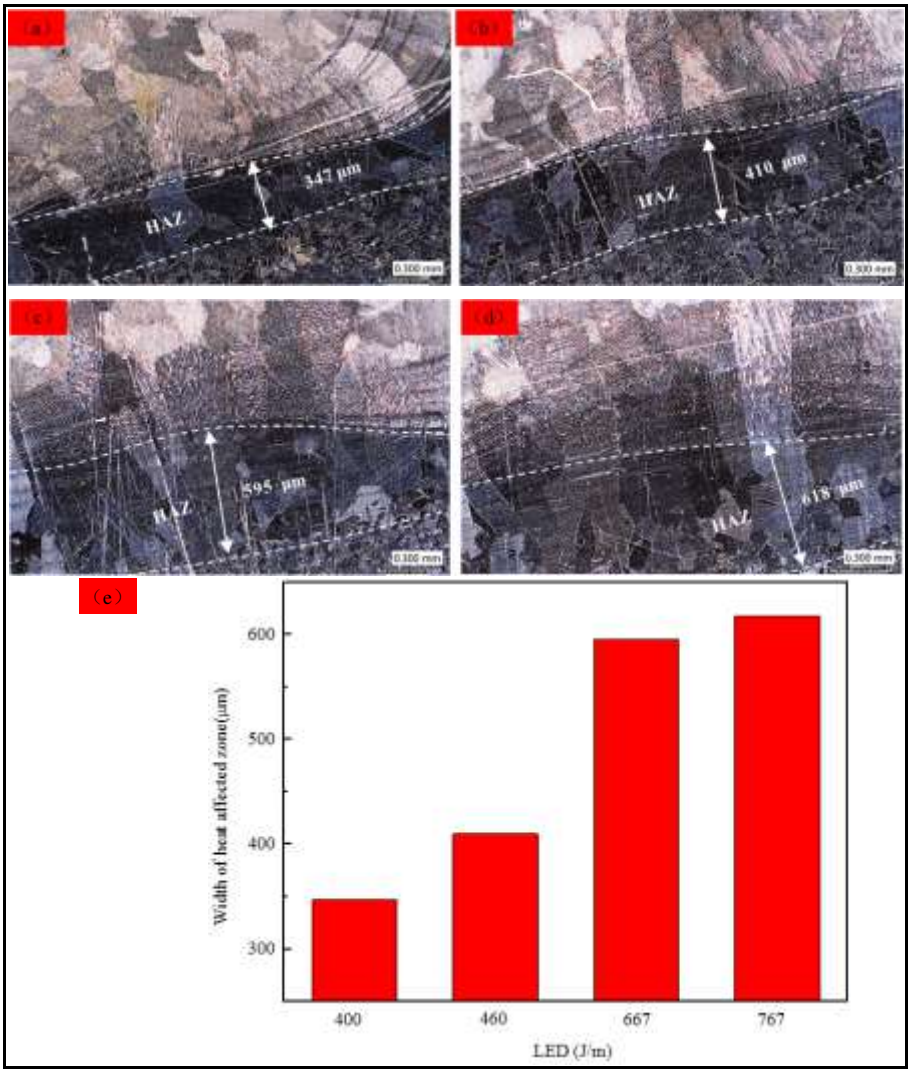

Fig. 8. HAZ microstructures with different processing parameters: (a) η_1=400 J/m; (b) η_2=460 J/m; (c) η_3=667 J/m; (d) η_4=767 J/m; (e) HAZ widths with different laser energy densities.

The average dendrite spacing of subgrains can be calculated using Equation 2:

$$\lambda = \frac{L}{N} \tag{2}$$

where L denotes the length of the measuring line and N is the number of cellular crystals. In this work, L was 100 μm, i.e. the length of three lines to measure the subgrain size.

The grain sizes of the columnar crystals at the bottom of molten pool with different processing parameters are shown in Fig. 9. With LED of 400 J/m, the average dendrite spacing of grains was 5.46 μm. When the LED increased to 460 J/m, the average dendrite spacing increased 1.52 μm, while when the LED increased to 667 J/m, the average dendrite spacing was 8.33 μm. When the LED was 767 J/m, the maximum average dendrite spacing was 9.09 μm. As shown in Fig. 9(e), the average dendrite spacing of grains increased with increase in LED. The cellular crystal is the internal subgrain structure in the columnar grains that grew epitaxially at the bottom of molten pool, which grew along the normal direction of the fusion line, i.e. the direction of the maximum temperature gradient. With an increase in the laser power or the reduction of scanning speed, the LED increased, the heat input increased, the powder energy absorption increased, the temperature of molten pool increased, the superheat of the alloy increased, the number of nucleation decreased, and the grains

grew sufficiently, which resulted in an increase in the average dendrite spacing. Meanwhile, an increase in the temperature gradient facilitated grain growth, which increased the average dendrite spacing.

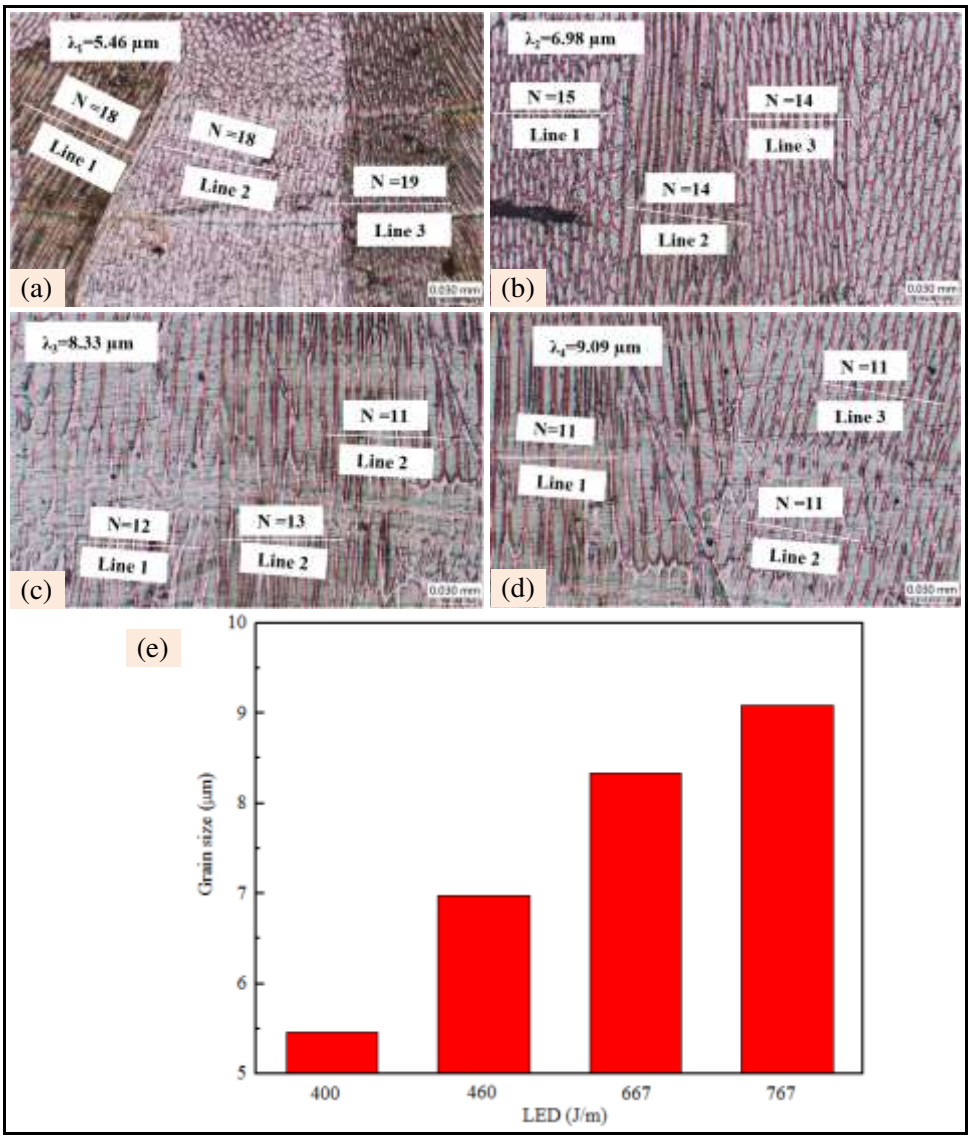

Fig. 9. Microstructures of center area of single-pass cladding layer molten pool with different processing parameters: (a) η_1=400 J/m; (b) η_2=460 J/m; (c) η_3=667 J/m; (d) η_4=767 J/m; (e) Grain sizes with different laser energy.

The grain size of regular equiaxed cellular crystals at the bottom of molten pool with different processing parameters can be measured with Image-Pro Plus 6.0 software. The obtained results are shown in Fig. 10. With an increase in LED, the grain size significantly increased. When LED was 400 J/m, the grain size of equiaxed cellular crystals was 4.78 μm. With LED increasing to 767 J/m, the grain size of the equiaxed crystals reached 7.86 μm. At lower LED, the heat input was less, the powder energy absorption was less, the temperature of molten pool was lower, and the cooling rate was higher, which increased the nucleation rate and accelerated the grain growth. However, the previous increased faster than the subsequent, which led to formation of fine grains. Meanwhile, owing to faster scanning speed, grains did not have enough time to grow, leading to smaller grain size.

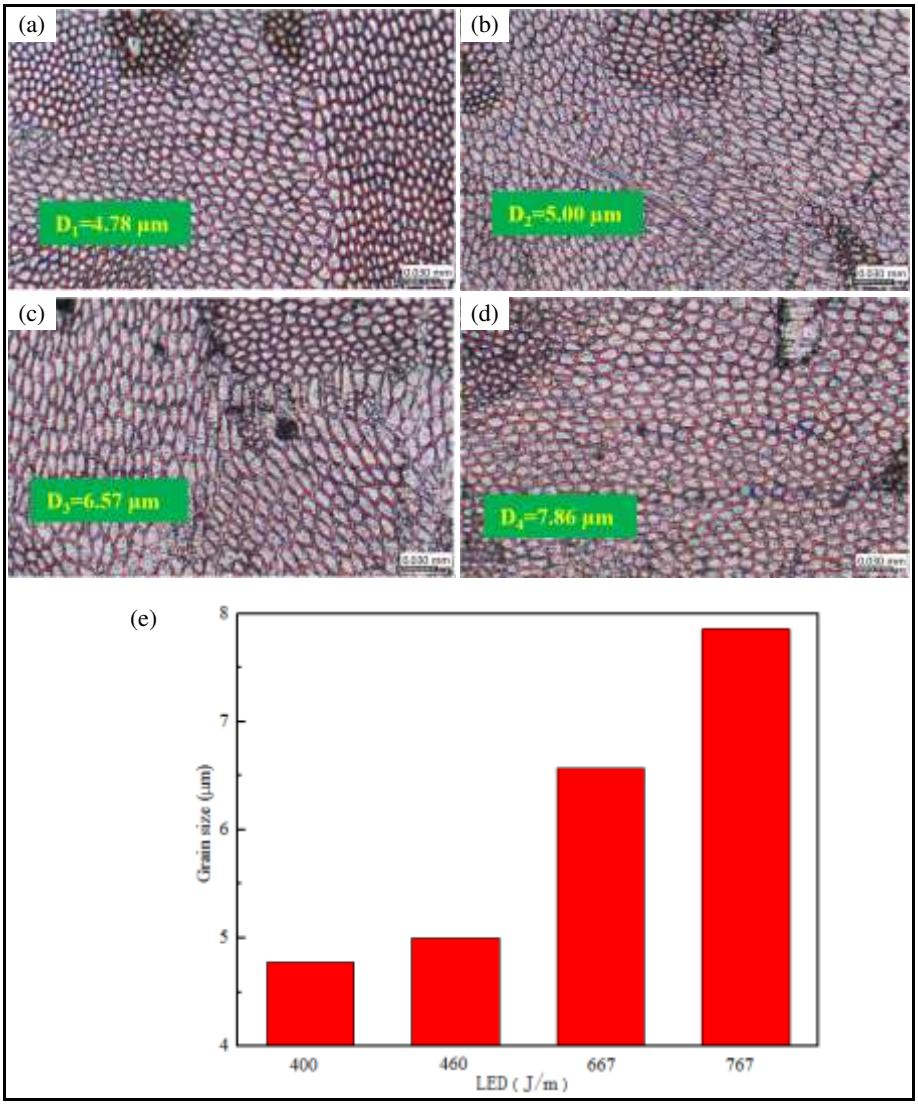

Fig. 10. Microstructures of bottom area of single-pass cladding layer molten pool with different processing parameters: (a) η_1=400 J/m; (b) η_2=460 J/m; (c) η_3=667 J/m; (d) η_4=767 J/m; (e) Grain sizes with different laser energy.

Microstructures of single-pass cladding samples with different processing parameters are shown in Fig. 11. The columnar crystals at the bottom of molten pool and equiaxed crystals at the top were divided, and the length of the columnar crystals was measured. With an increase in LED, the length of columnar crystals continuously increased and the distribution proportion between equiaxed crystal area and columnar crystal area increased. As displayed in Fig. 11, there was a clear boundary between the columnar crystals at the bottom and equiaxed crystals at the top. At LEDs of 400 J/m, 460 J/m, 667 J/m, and 767 J/m, the corresponding lengths of columnar crystals were 652 μm, 991 μm, 1100 μm, and 1104 μm, respectively. There was a competitive growth relationship within the grains in the cladding layer. The lower the power was, the lower the temperature of molten pool was and the smaller the temperature gradient was. This phenomenon benefitted the nucleation and growth of equiaxed crystals and suppressed the growth of columnar crystals, which increased the distribution proportion between the equiaxed crystal area and columnar crystal area. The increase in scanning speed promoted the growth of equiaxed crystals and suppressed further growth of columnar crystals. Meanwhile, shortening of solidification time suppressed further development

of columnar crystals, which increased the distribution proportion between equiaxed crystal area and columnar crystal area.

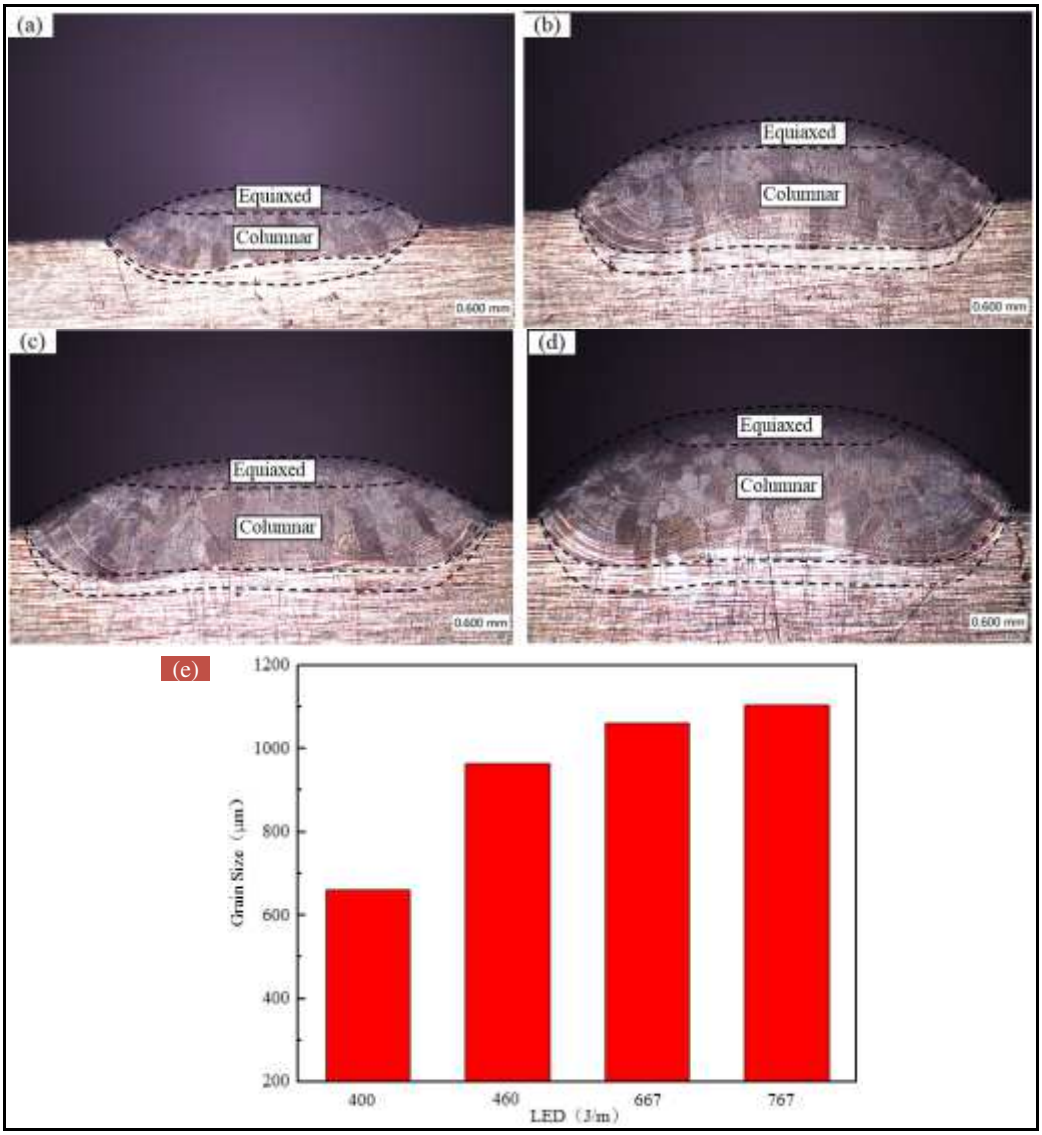

Fig. 11. Microstructure of single-pass cladding layers with different processing parameters: (a) η_1=400 J/m; (b) η_2=460 J/m; (c) η_3=667 J/m; (d) η_4=767 J/m; (e) the length of columnar crystals with different laser energy.

According to the measure in Fig. 7, EDS elemental measurements were conducted on the samples at the speed of 3 mm/s, feeding rate of 1.5 g/s, and power of 2000 W and 2300 W. The corresponding results are shown in Table 4. With an increase in power, the maximum and minimum Fe contents of each measured point significantly increased. Also, the elemental content difference between the near edge region and near central region gradually increased with the laser power. It is because with an increase in the laser power, both the surface temperature gradient of molten pool and surface tension gradient increased; therefore, the Marangoni convection intensity accordingly increased. The increased convection intensity made the component transfer more clear. Meanwhile, the elemental accumulation phenomenon at the edge of molten pool accordingly enhanced, which led to relatively large elemental difference between the edge region and central region with high power.

Table 4 Measured results of Fe contents with different powers

Laser power /W	Point 1 (%)	Point 2 (%)	Point 3 (%)	Point 4 (%)	Point 5 (%)	Point 6 (%)
2000	63. 61	63.86	63.98	63.59	63.45	63.42
2300	64.39	64.25	64.35	62.86	62.52	63.38

3.3 Effects of heat accumulation on microstructure

In the multi-pass cladding, the heat generated by the previous cladding layer transferred to the subsequent cladding layer, which resulted in the heat accumulation effect. The heat accumulation effect had significant impact on the microstructure cladding layers, mainly including the HAZ width, grain size, and remelting zone size.

During the multi-pass laser cladding, the HAZ widths of different cladding layers are shown in Fig. 12. With the increase in cladding passes, the HAZ width continuously increased. The HAZ width of first laser cladding pass was 582.16 μm, while that for the second pass was 678.26 μm. The maximum width of HAZ reached 878.26 μm at fifth pass. The heat generated by the previous pass preheats the subsequent pass, leading to the heat accumulation effect. The phenomenon makes the temperature of the subsequent pass higher than that of the previous one. The increasing pass led to the increasing heat accumulation effect, a continuous increase in temperature, higher free energy of grain boundaries, easier grain boundary movement, more serious grain absorption, and hence, the grain coarsening and larger HAZ width.

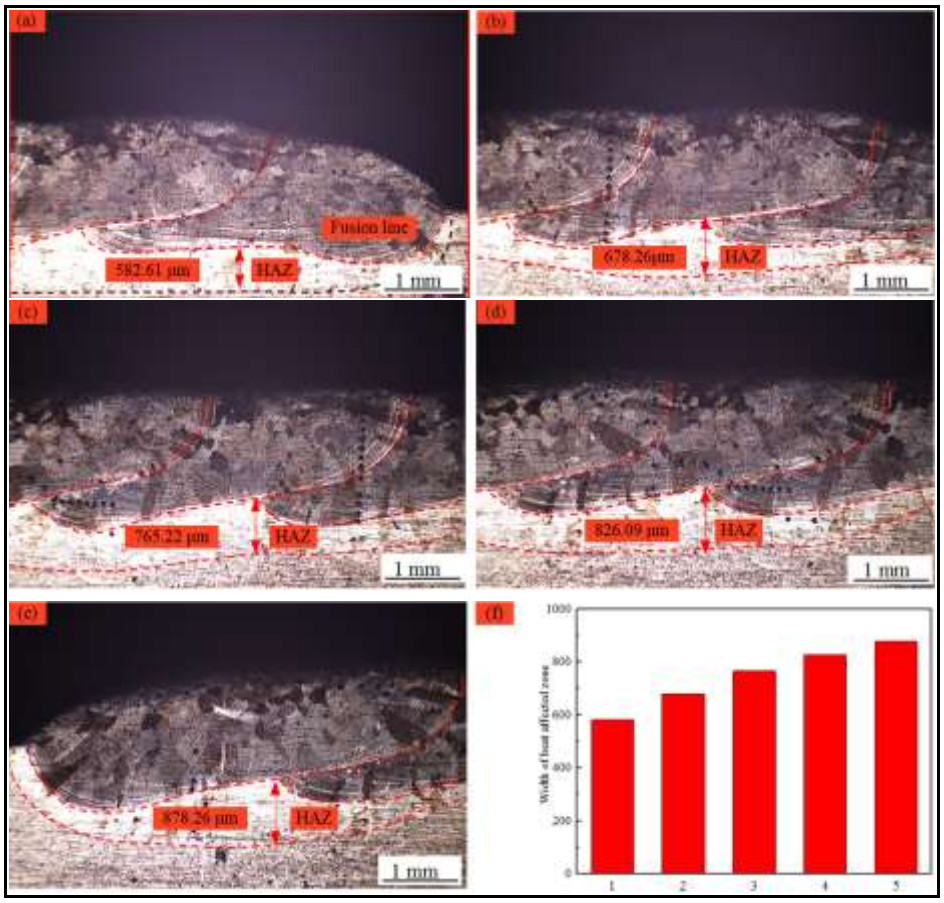

Fig. 12. Multiple overlaps of cladding layer: (a) the first pass HAZ width; (b) the second pass HAZ width; (c) the

third pass HAZ width; (d) the fourth pass HAZ width; (e) the fifth pass HAZ width; (f) HAZ widths of different cladding layers.

The subgrain size in the columnar crystals at the bottom of different cladding layers can be calculated by Equation 3:

$$D = 2\sqrt{\frac{d^2}{n\pi}} \tag{3}$$

where D is the subgrain size, d is the length of the measuring square, and n is the number of cellular crystals. The square with the length, d, of 50 μm was used to measure the subgrain size.

In the multi-pass cladding layers, the subgrain sizes in columnar crystals at the bottom of molten pool of different cladding layers are shown in Fig. 13. With an increase in the cladding passes, the subgrain size at the bottom of molten pool continuously increased. Compared to the subgrain size of 6.79 μm at the bottom of the first pass, the subgrain size for the fifth pass significantly increased to 12.03 μm. This is because with an increase in scanning passes, the heat accumulation effect increased, temperature of melting path increased, and cooling rate was lower, which led to lower nucleation rate. Meanwhile, at higher temperatures, the grains had enough driving force to sufficiently grow, and hence, larger subgrain size.

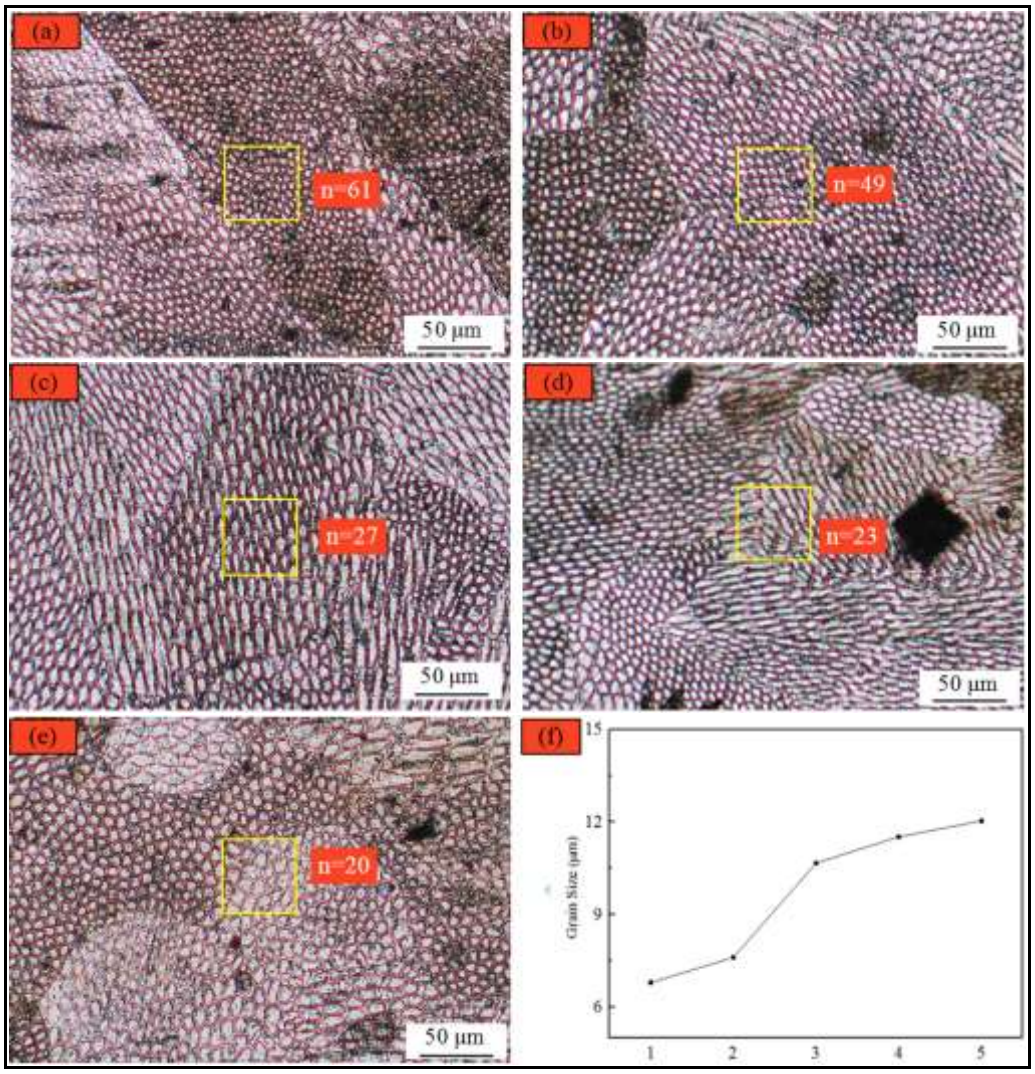

Fig. 13. Multiple overlaps of the cladding layer: (a) the first pass cross-sectional grain size; (b) the second pass cross-sectional grain size; (c) the third pass cross-sectional grain size; (d) the fourth pass cross-sectional grain size; (e) the

fifth pass cross-sectional grain size; (f) grain sizes of equiaxed cellular crystals at molten pool bottoms of different cladding layers.

During multi-pass cladding process, the subsequent cladding layer partially remelted the previous formed cladding layer, which mixed and co-solidified, and the new cladding layer was formed. The remelting zone represents the bonding degree between pass and pass, and the good bonding between pass and pass represents the appropriate overlapping rate. The remelting zone is shown in Fig. 14(a). The remelting zones of different cladding layers are shown in Fig. 14(b). With an increase in scanning pass, the remelting zone continuously increased. From the second pass to the fifth pass, the width of remelting zone increased from 1.40 mm to 3.09 mm, and the height of remelting zone increased from 1.59 mm to 2.02 mm. This phenomenon is primarily because of the heat accumulation effect. With an increase in the cladding pass, the molten pool temperature was higher, which made the sufficiently melted the path, leading to a larger remelting zone.

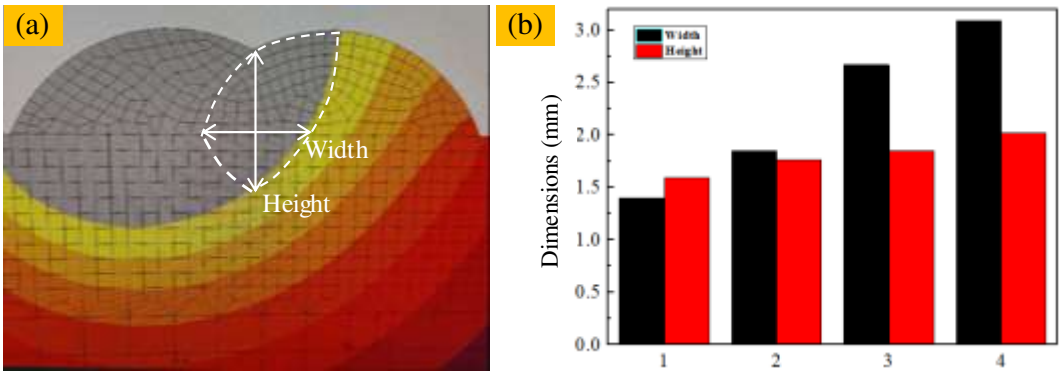

Fig. 14. Multiple overlaps of cladding layer: (a) schematic of remelting zone of cladding layer; (b) remelting zone of different cladding layers.

3.4 Microhardness analysis

For the single-pass cladding sample processed with the power of 2000 W, speed of 3 mm/s, and feeding rate of 1.5 g/s, the microhardness variation from the top of cladding layer to the substrate is displayed in Fig. 15. Fig. 15(a) shows the schematic of each microhardness measuring point. As presented in Fig. 15(b), the microhardness at the top of cladding layer reached ~199.9 $HV_{0.2}$. The microhardness at the center of the cladding layer decreased, ~~165.7 $HV_{0.2}$, while the microhardness value at the bottom of cladding layer reduced to ~157.3 $HV_{0.2}$. However, the microhardness values from HAZ to substrate increased from 135 $HV_{0.2}$ to 158.8 $HV_{0.2}$. Therefore, the rule can be drawn as follows: along the center line of the cladding layer (gradually approaching to the bottom of the cladding layer), the microhardness gradually decreased. Upon reaching the HAZ, the microhardness reached the minimum value, which then increased at the substrate.

The microhardness variation in different zones in the cladding layer was mostly affected by the grain size. In the cladding layer, it primarily included the equiaxed crystal zone at the top and the columnar crystal zone at the bottom. Because the grains at the top were melted and cooled more rapidly, the grains at the top were finer than those at the bottom, which resulted in higher microhardness at the top. Because of continuous heat effect of the central and bottom parts of the cladding layer, the grains were gradually coarser compared with those at the top, and hence, a lower microhardness value. The microhardness reduction in HAZ was caused by the austenite grain coarsening. The austenite grain growth reduced the resistance to plastic deformation of grains,

leading to a reduction in the microhardness. The austenite grain of the substrate was relatively fine. Thus, the microhardness of this region was higher than that in the HAZ.

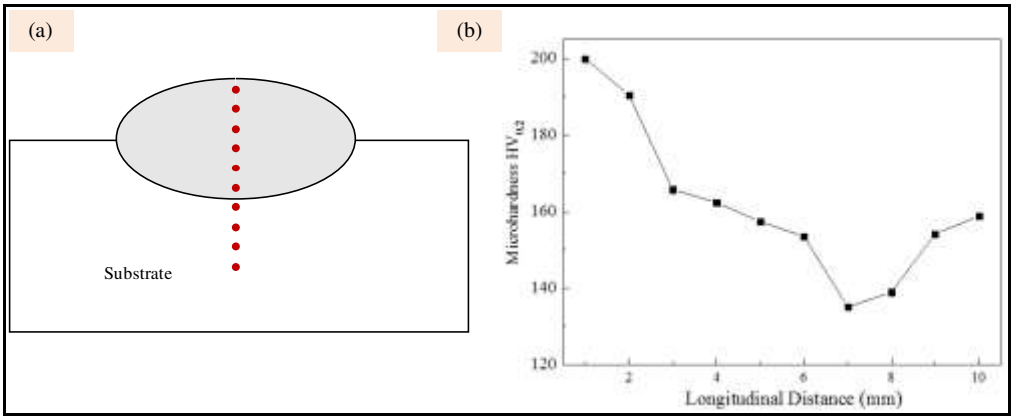

Fig. 15. Microhardness from the top to bottom of the cladding layer: (a) distribution schematic of microhardness; (b) microhardness values.

Fig. 16 shows the microhardness values of multi-pass samples along the horizontal direction. Fig. 16(a) shows the schematic of the microhardness measuring points in the first pass, second pass, and remelting zones. As per Fig. 16(b), the microhardness in the center of the first pass reached the maximum value of 285.9 $HV_{0.2}$, and it gradually decreased along the horizontal direction. Finally, the minimum value of 253.8 $HV_{0.2}$ was obtained at the remelting zone. The microhardness gradually increased in second pass, and it reached ~282.0 $HV_{0.2}$ at the center, which was lower than that in the first pass (285.9 $HV_{0.2}$). Thus, the rule along the horizontal direction is as follows: the microhardness of the cladding layer in the previous pass was higher than that in the subsequent pass. The microhardness significantly decreased in the remelting zone. The effect of heat accumulation made the grains in the subsequent cladding zone coarser than those in the previous cladding zone, which led to lower microhardness. Meanwhile, the grains in remelting zone grew intensely, leading to severe grain growth and significant microhardness reduction.

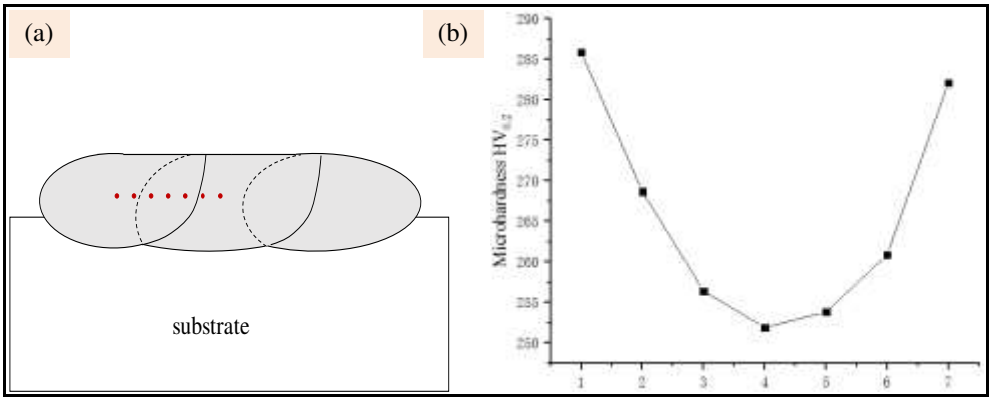

Fig. 16. Microhardness of multi-pass cladding layers: (a) distribution schematic of microhardness measuring points; (b) microhardness values.

4. Conclusions

1. The cladding layer of Invar alloy consists of the columnar crystals at the bottom, and equiaxed crystals at the top. In the initial solidification stage, the grain growth conditions are sufficient,

and the grains continuously grow perpendicular to the fusion line. Meanwhile, enough space allows for sufficient growth along the width direction. However, later on at the solidification stage, the grain growth space is limited with shrinkage of the molten pool. The grain growth is slowed down, and even the CET occurs.

2. The increase of laser energy expands the width of grain size, the HAZ, the distribution ratio of equiaxed crystal region compared with the columnar crystal, and the difference in the element content of the near-edge region and the near-center region.
3. when the multi-pass overlaps, the heat accumulation effect generated by the previous cladding layer transfers to the subsequent, in turn increases the HAZ width, grain size, and remelting zone.
4. The grain at the top of cladding layer is finer than that at the bottom, so the microhardness of the top higher than that of the bottom. The coarsening of austenite grain in the HAZ leads to the microhardness decrease significantly. In addition, the heat accumulation effect results in the grains of the subsequent cladding layer coarser and the hardness lower than the previous.

Ethical Approval The article follows the guidelines of the Committee on Publication Ethics (COPE) and involves no studies on human or animal subjects.

Consent to Participate Not applicable.

Consent to Publish Not applicable.

Authors Contributions Shichao Zhu conceived the analysis and wrote the manuscript. Chenxiao Yu collected the data and revised the manuscript. Zhen Chang worked laser cladding experiments. Chao Zeng measured cladding layer of microstructure. Xiaohong Zhan provided experimental equipment, experimental materials and experimental expenses.

Funding The authors gratefully acknowledge the State Key Laboratory of Additive Manufacturing, China academy of engineering physics (Granted No. ZM17002), the Natural Science Foundation of the Jiangsu Higher Education Institutions of China (Granted No.19KJA430005) and Guizhou Provincial Science and Technology Foundation Grant (Granted No. 20191415).

Competing Interests The authors declare that they have no competing interests.

Availability of data and materials All data generated or analyzed during this study are included in the present article.

References

1. Gu D D, Meiners W, Wissenbach K, R Poprawe (2013) Laser additive manufacturing of metallic components: materials, processes and mechanisms. Int Mater Rev 57(3): 133-164.
2. Penaranda X, Moralejo S, Lamikiz A, et al (2017) An adaptive laser cladding methodology for blade tip repair. Int J Adv Manuf Technol 92(10): 4337-4343.
3. Sexton L, Lavin S, Byrne G, Kennedy (2002) A. Laser cladding of aerospace materials. Journal of Materials Processing Tech 122(1): 63-68.
4. Torres E A, Apolinario L, Araujo H R, et al (2021) Banding and microstructural features in laser cladding of a 304 substrate using 316 powder Int J Adv Manuf Technol 112(7-8): 2327-2339.
5. Farshidianfar M H, Khajepour A, Gerlich A (2016) Real-time control of microstructure in laser additive manufacturing. Int J Adv Manuf Technol 82(5-8): 1173-1186.

6. Penaranda X, Moralejo S, Lamikiz A, Figueras J (2017) An adaptive laser cladding methodology for blade tip repair. Int J Adv Manuf Technol 92(3): 1-7.
7. Yu J, Kim D (2018) Effects of welding current and torch position parameters on minimizing the weld porosity of zinc-coated steel. Int J Adv Manuf Technol 95(1-4): 551-567.
8. Mohammed S, Zhang Z, Kovacevic R (2020) Optimization of processing parameters in fiber laser cladding. Int J Adv Manuf Technol 111(12): 2553-2568.
9. Lian G, Zhang H, Zhang Y, et al (2020) Control and prediction of forming quality in curved surface multi-track laser cladding with curve paths. Int J Adv Manuf Technol 106(9-10):3669-3682.
10. Moralejo S, Penaranda X, Nieto S, et al (2017) A feedforward controller for tuning laser cladding melt pool geometry in real time. Int J Adv Manuf Technol 89(3): 821-831.
11. Zhang K, Li D, Gui H, et al (2019) An adaptive slicing algorithm for laser cladding remanufacturing of complex components. Int J Adv Manuf Technol 101(4): 2873-2887.
12. Zhang Z, Kovacevic R (2019) A thermo-mechanical model for simulating the temperature and stress distribution during laser cladding process. Int J Adv Manuf Technol 102(5): 457-472.
13. Deng D W, Sun J H, Wang X L, Zhang H C (2016) Laser Power Effect on Microstructure and Property of Laser Cladding Nickel Based Alloy Coating. Chinese journal of rare metals 40(1): 20-25.
14. XU B S, Fang J X, Dong S Y, Liu X T, Yan S X (2016) Heat-affected zone microstructure evolution and its effects on mechanical properties for laser cladding FV520B stainless steel. Acta metallurgica sinica 52(1): 1-9.
15. Zhan X H, Qi C Q, Gao Z N, Tian D Y, Wang Z D (2019) The influence of heat input on microstructure and porosity during laser cladding of Invar alloy. Optics and Laser Technology 113(5): 453–461.
16. Dinda G P, Dasgupta A K, Mazumder J (2009) Laser aided direct metal deposition of Inconel 625 superalloy: Microstructural evolution and thermal stability. Materials Science & Engineering 509(1-2): 98-104.
17. Zhan X H, Meng Y, Zhou J J, Qi C Q, Zhang C L, Gu D D (2018) Quantitative research on microstructure and thermal physical mechanism in laser melting deposition for Invar alloy. Journal of Manufacturing Processes 31(1): 221–231.
18. Amine T, Newkirk J W, Liou F (2014) An investigation of the effect of laser deposition parameters on characteristics of multilayered 316. Int J Adv Manuf Technol 73(9-12): 1739-1749.

Figures

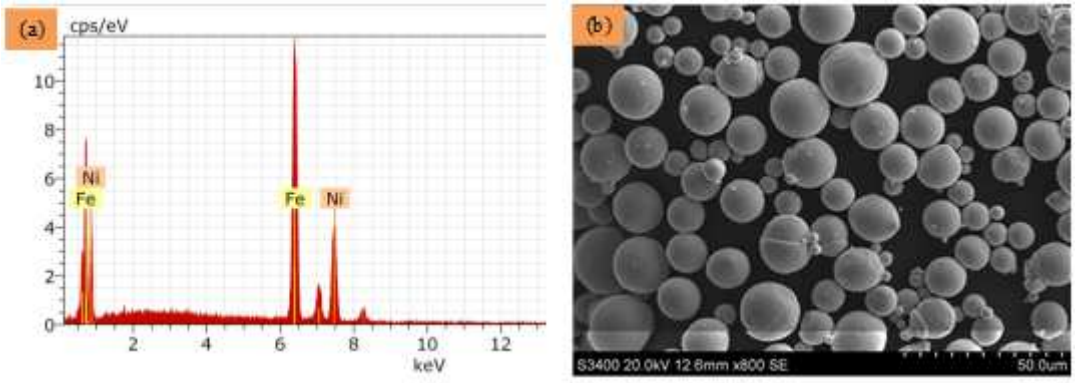

Figure 1

Elemental composition and morphology of Invar alloy particles. (a) Elemental composition. (b) Morphology

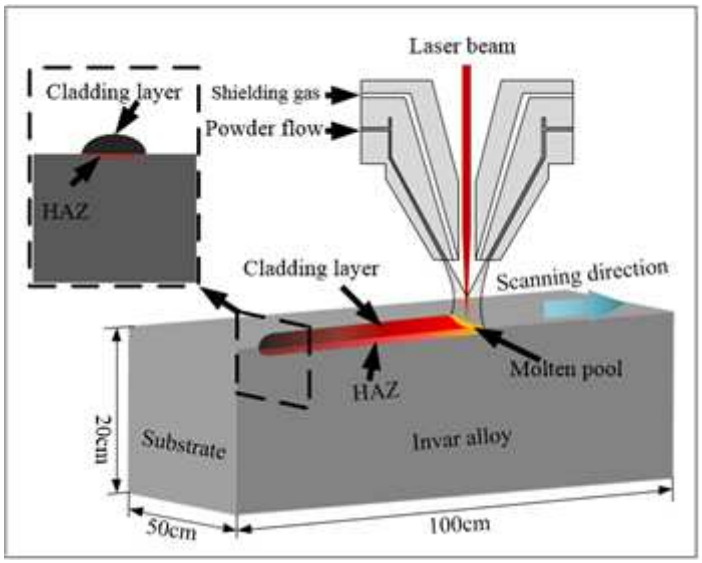

Figure 2

Diagrammatic of LCR process

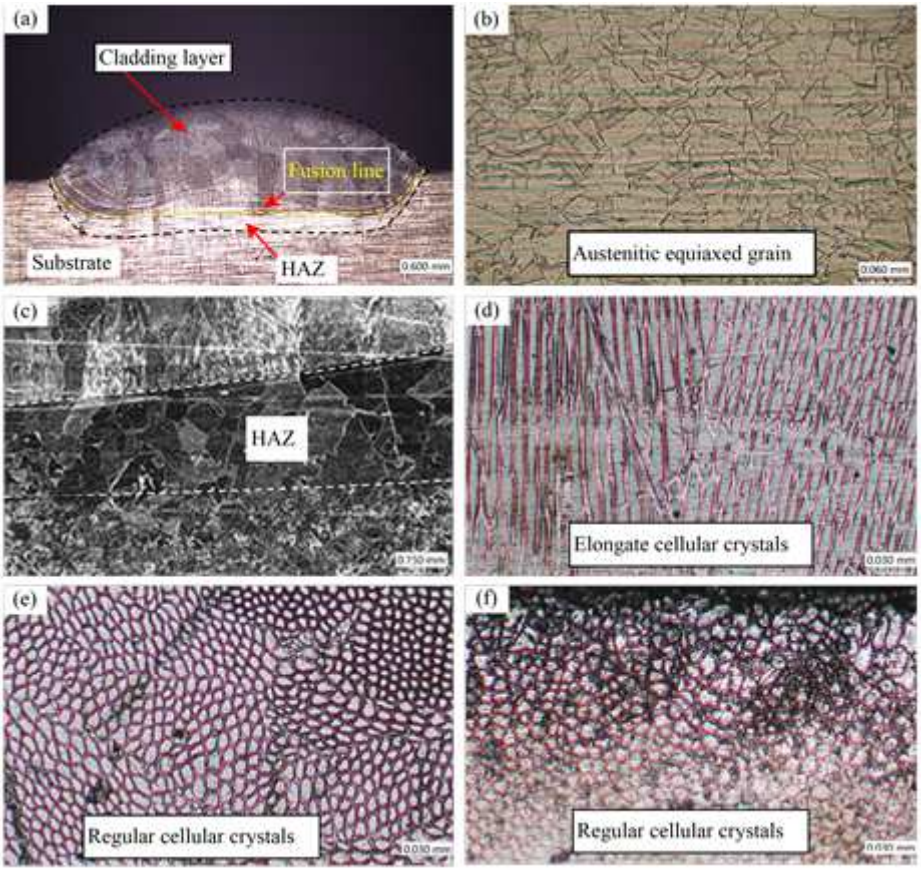

Figure 3

Microstructures of different regions of single-pass cladding layer cross section: (a) cross-sectional microstructure; (b) substrate microstructure; (c) HAZ microstructure; (d) microstructure at the bottom region of cladding layer; (e) microstructure at the bottom region of cladding layer; (f) microstructure at the top region.

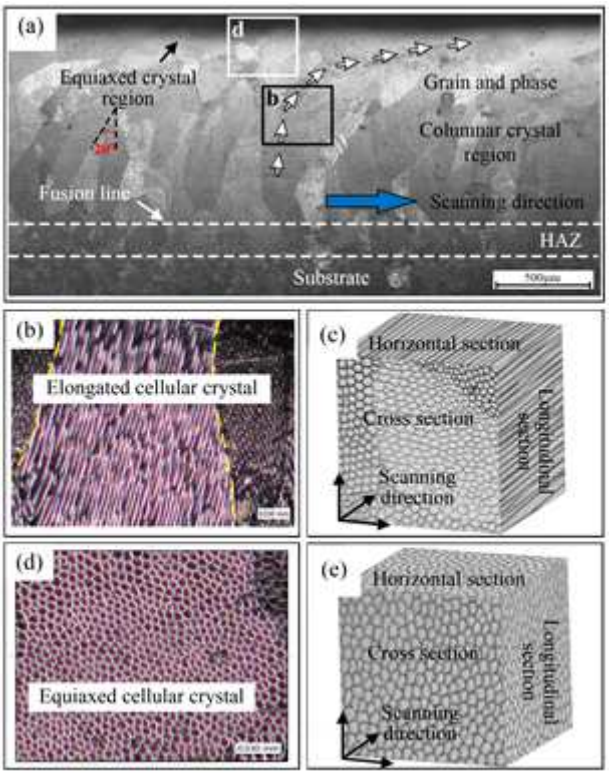

Figure 4

Microstructure of longitudinal section of the cladding layer: (a) microstructure of longitudinal section; (b) microstructure of the central region; (c) 3-dimensional image of subgrains in the central region; (d) microstructure at the top region; (e) 3-dimensional image of subgrains at the top region.

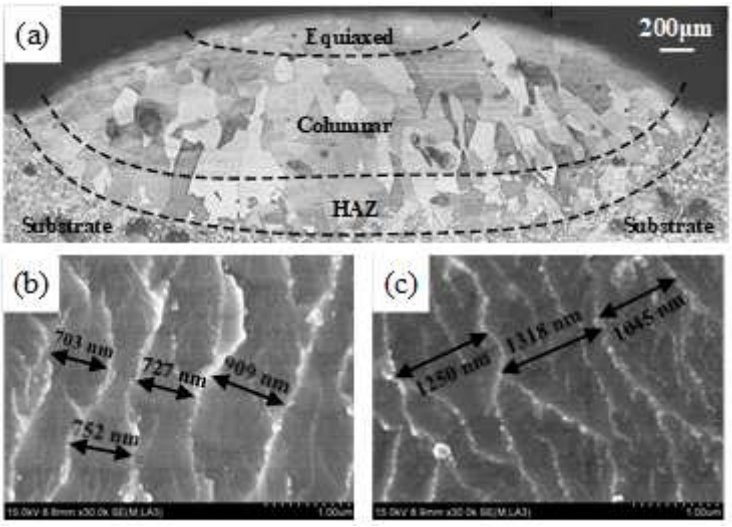

Figure 5

SEM images of top and bottom of the cladding layer cross section: (a) Microstructure images; (b) SEM micrograph of top grains; (c) SEM micrograph of bottom grains.

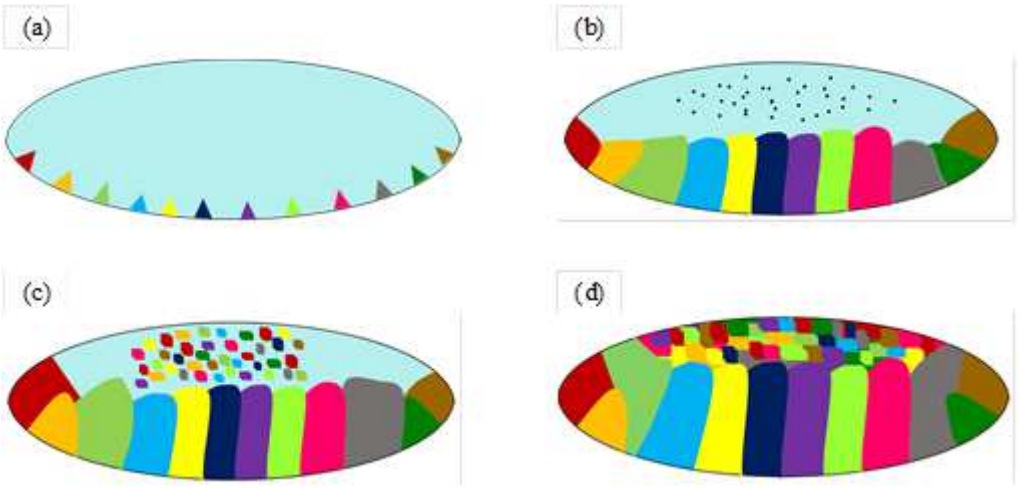

Figure 6

Columnar-to-equiaxed transition (CET) process.

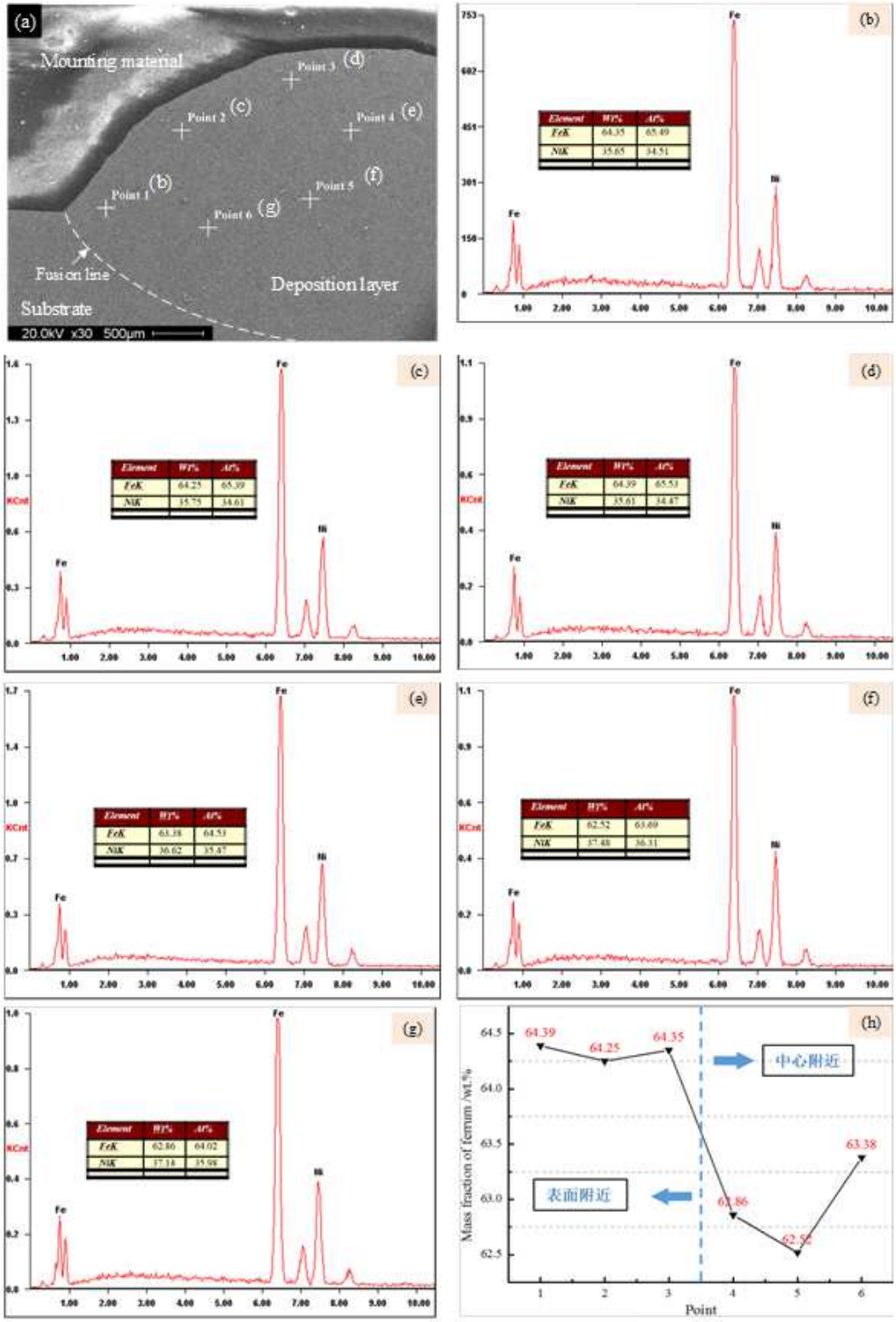

Figure 7

EDS elemental measuring results of the cladding layer cross section: (a) schematic diagram; (b) – (g) results of different measuring points; (h) variation curve of Fe content

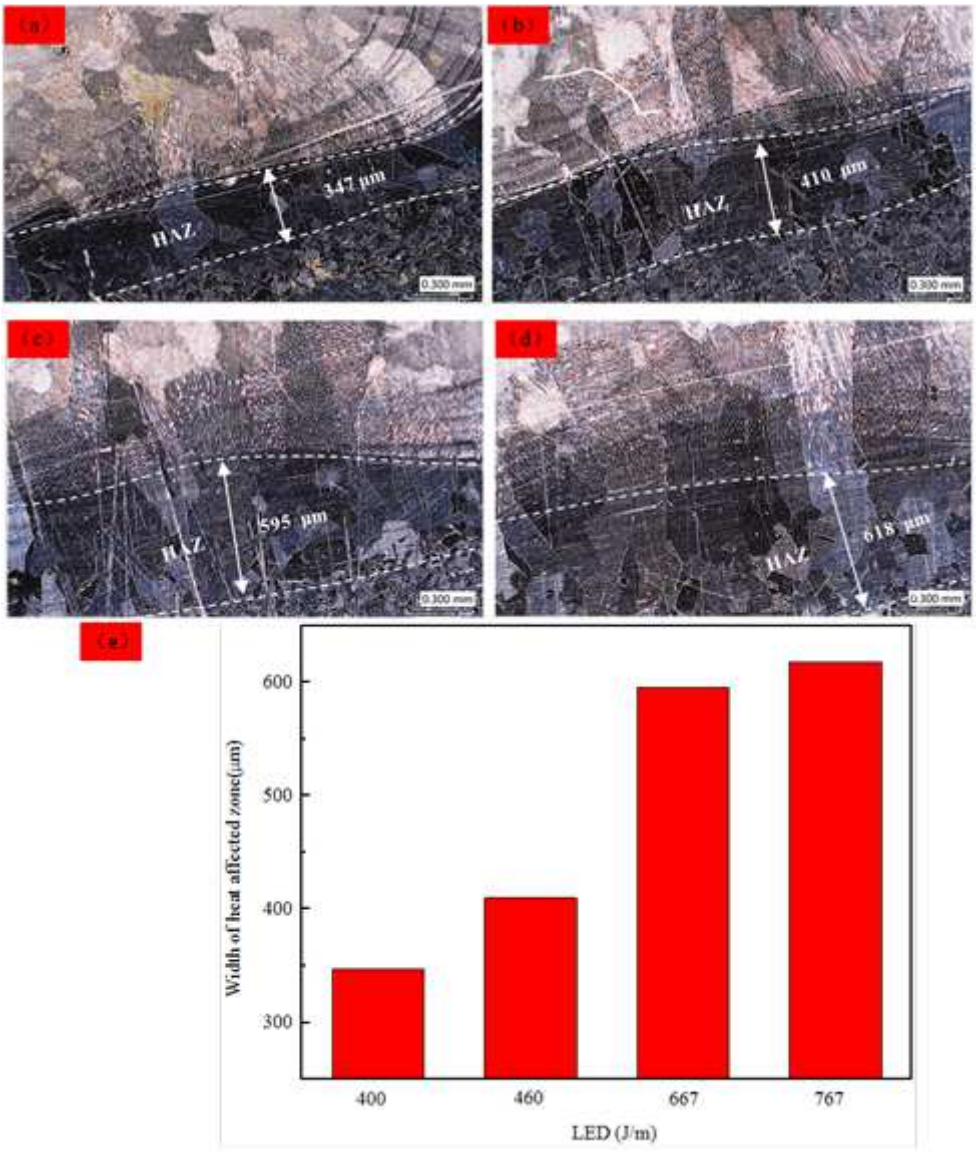

Figure 8

HAZ microstructures with different processing parameters: (a) η1=400 J/m; (b) η2=460 J/m; (c) η3=667 J/m; (d) η4=767 J/m; (e) HAZ widths with different laser energy densities.

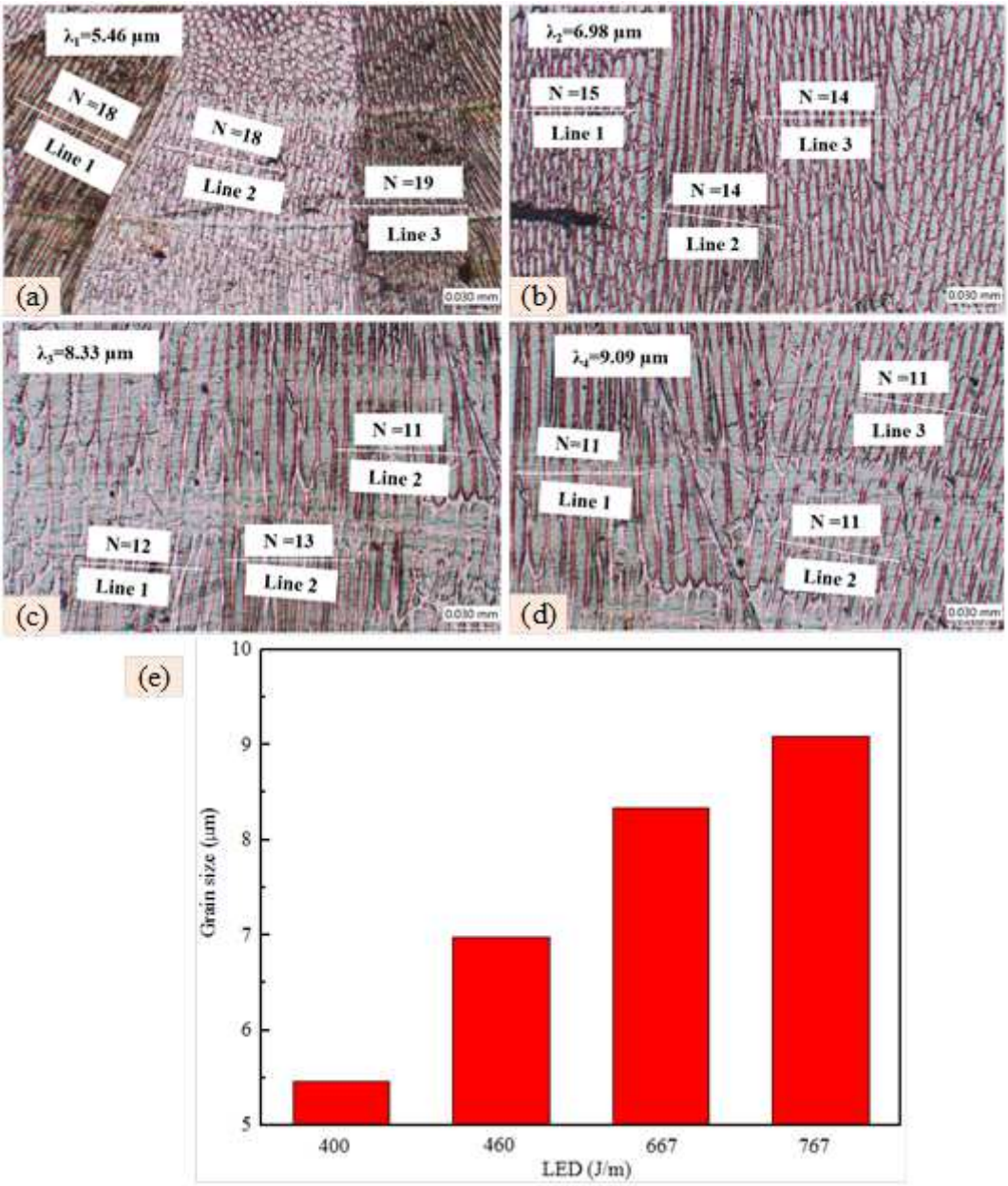

Figure 9

Microstructures of center area of the single-pass cladding layer molten pool with different processing parameters: (a) η1=400 J/m; (b) η2=460 J/m; (c) η3=667 J/m; (d) η4=767 J/m; (e) Grain sizes with different laser energy.

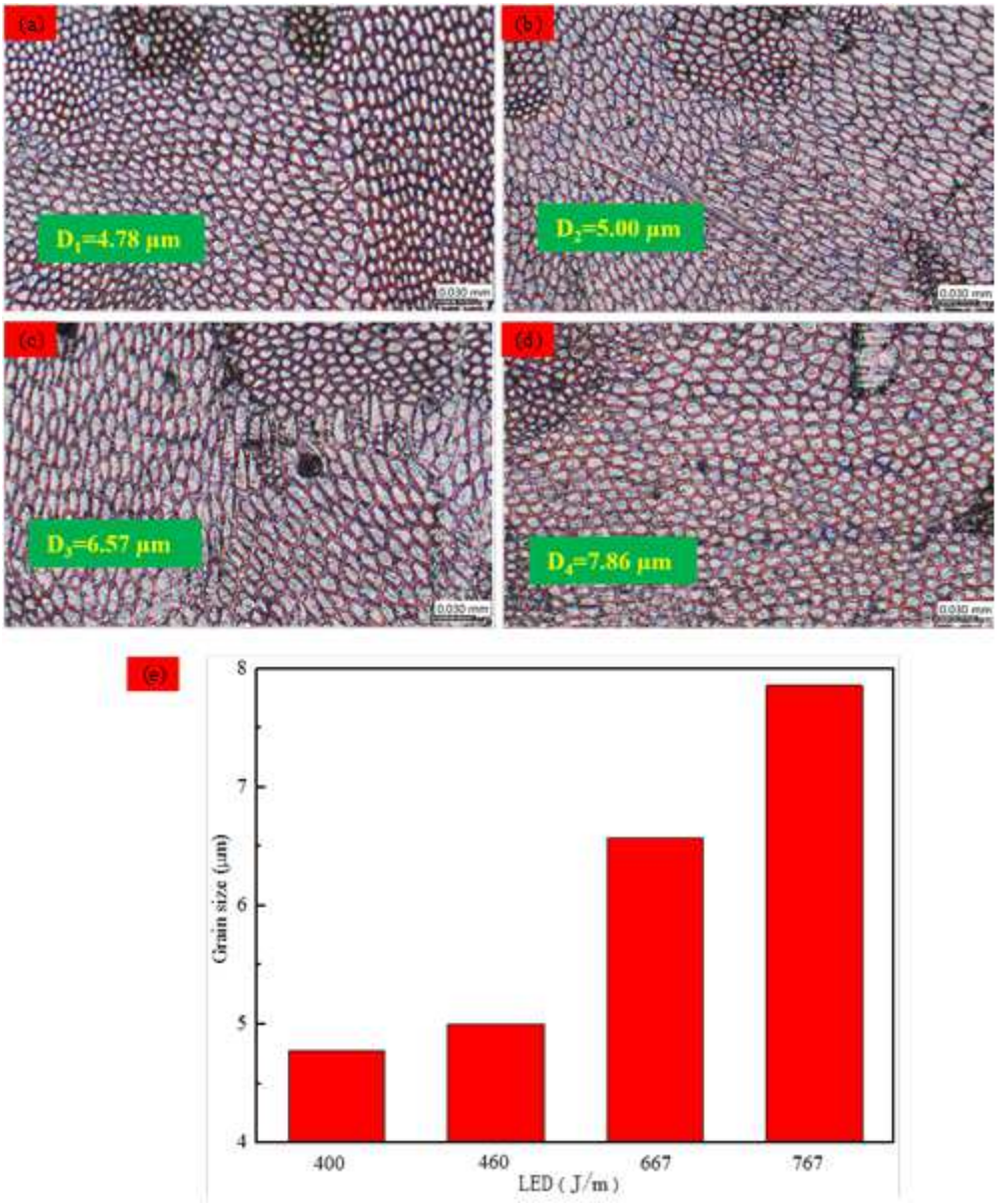

Figure 10

Microstructures of bottom area of single-pass cladding layer molten pool with different processing parameters: (a) η1=400 J/m; (b) η2=460 J/m; (c) η3=667 J/m; (d) η4=767 J/m; (e) Grain sizes with different laser energy densities.

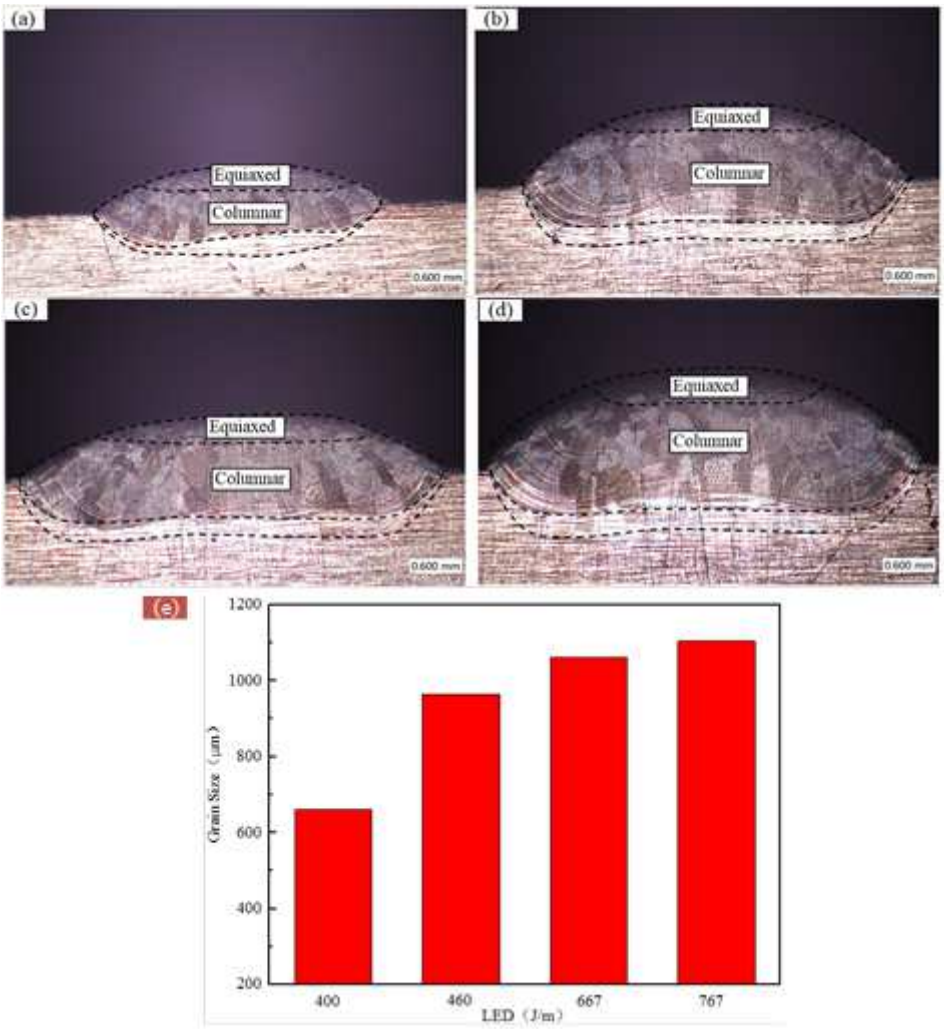

Figure 11

Microstructure of the single-pass cladding layers with different processing parameters: (a) η1=400 J/m; (b) η2=460 J/m; (c) η3=667 J/m; (d) η4=767 J/m; (e) the length of columnar crystals with different laser energy densities.

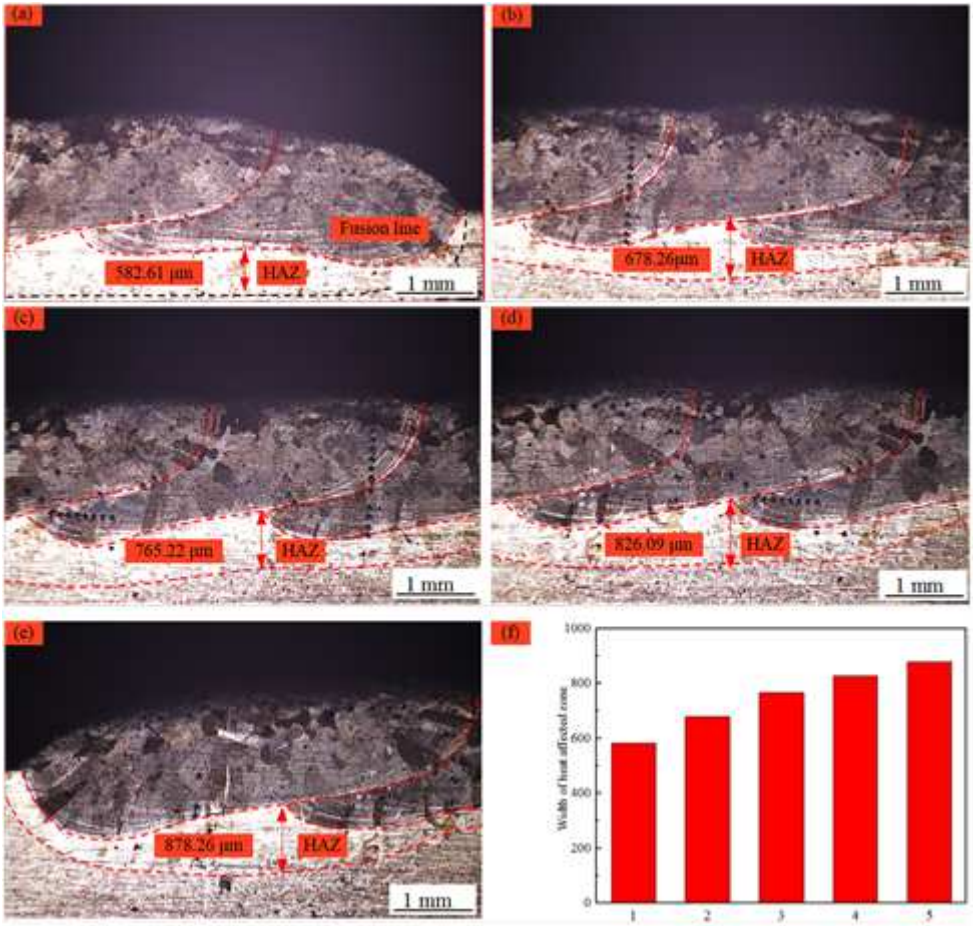

Figure 12

Multiple overlaps of cladding layer: (a) the first pass HAZ width; (b) the second pass HAZ width; (c) the third pass HAZ width; (d) the fourth pass HAZ width; (e) the fifth pass HAZ width; (f) HAZ widths of different cladding layers.

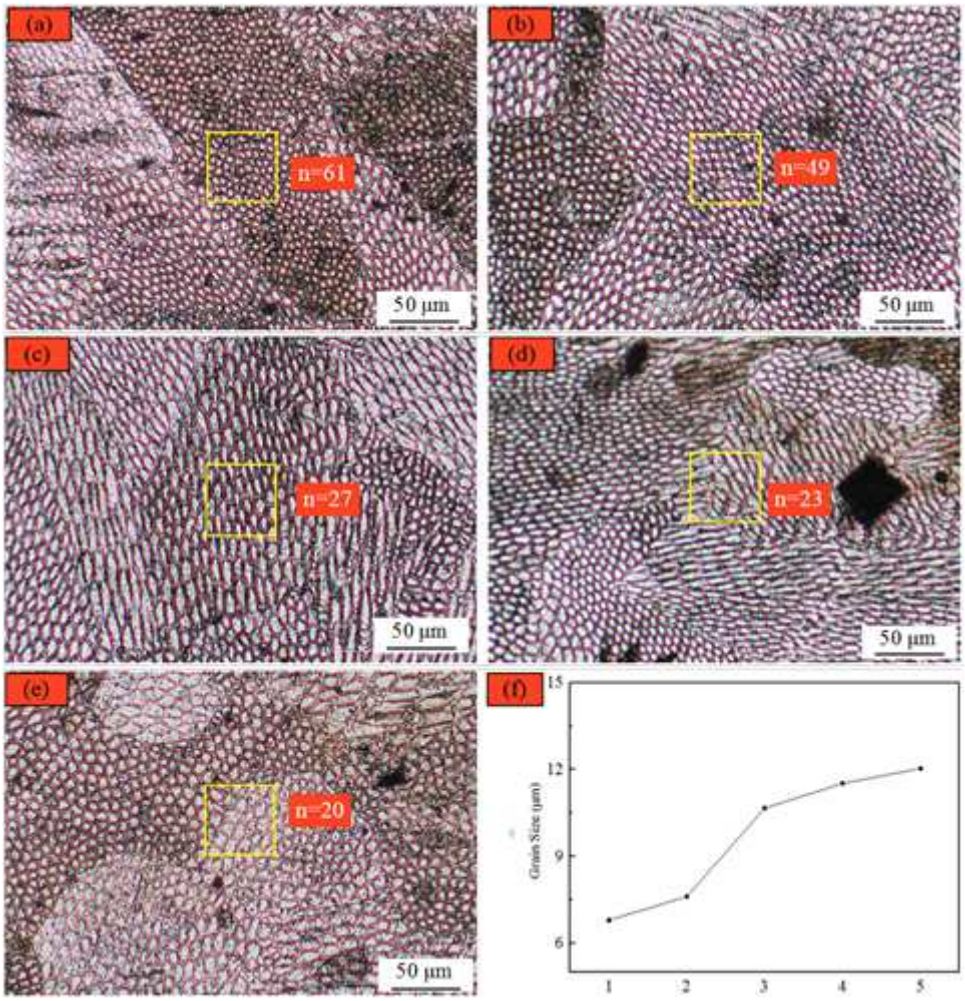

Figure 13

Multiple overlaps of the cladding layer: (a) the first pass cross-sectional grain size; (b) the second pass cross-sectional grain size; (c) the third pass cross-sectional grain size; (d) the fourth pass cross-sectional grain size; (e) the fifth pass cross-sectional grain size; (f) grain sizes of equiaxed cellular crystals at molten pool bottoms of different cladding layers.

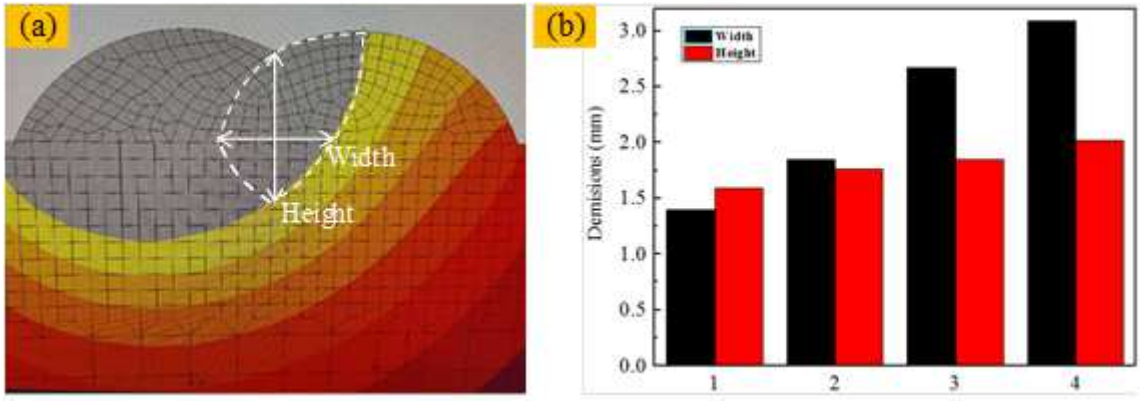

Figure 14

Multiple overlaps of the cladding layer: (a) schematic of remelting zone of cladding layer; (b) remelting zone of different cladding layers.

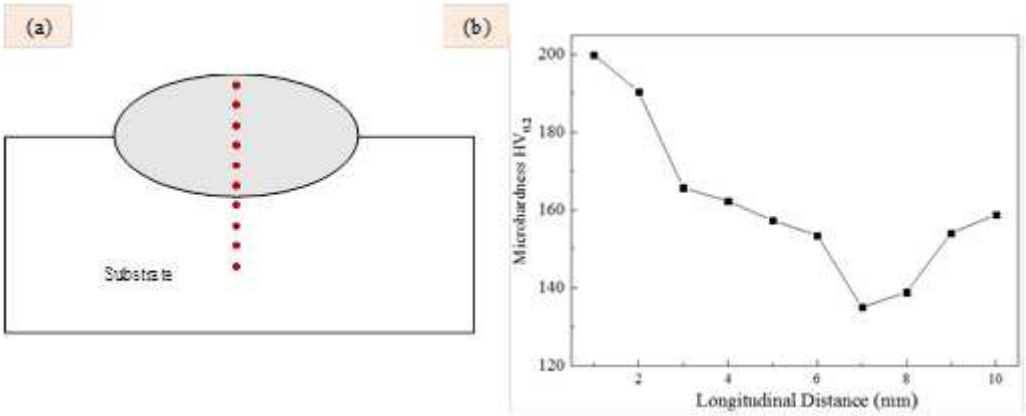

Figure 15

Microhardness from the top to bottom of the cladding layer: (a) distribution schematic of microhardness; (b) the microhardness values.

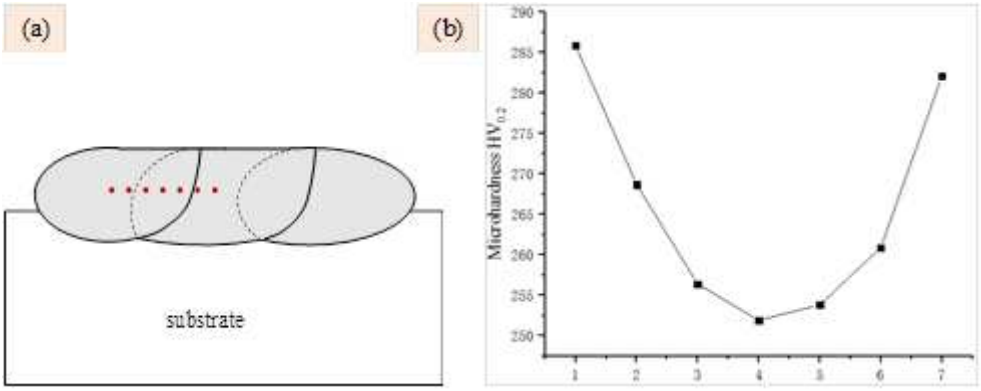

Figure 16

Microhardness of multiple overlapped cladding layer: (a) distribution schematic of microhardness measuring points; (b) microhardness values.